https://doi.org/10.5194/egusphere-2026-836
Preprint. Discussion started: 12 March 2026

Summertime ozone sensitivity to temperature in China: observational evidence and mechanistic attribution in urban and rural areas in the Yangtze River Delta region

Chang Su[1], Massimo Bollasina[1], James Weber[2], David Stevenson[1]

[1]School of GeoSciences, University of Edinburgh, Edinburgh, UK
[2]Department of Meteorology, University of Reading, Reading, UK

Correspondence to: Chang Su (Chang.Su@ed.ac.uk)

Abstract. As climate change increases frequency and intensity of hot extremes, understanding how elevated temperatures influence surface ozone (O_3) across different chemical regimes is critical. We combine observations from summer 2022 in the Yangtze River Delta (YRD) with targeted United Kingdom Chemistry and Aerosols (UKCA) Box experiments to quantify and attribute the temperature sensitivity of ground-level O_3 in a VOC-limited urban megacity (Shanghai) and a predominantly NO_x-limited rural region (Lishui). Observed daily-maximum O_3 increases with temperature at both sites, with a stronger response in Shanghai. Two-dimensional T-RH distributions show that O_3 rises with temperature and decreases with relative humidity (RH), implying that part of the temperature response is mediated by drying. Factorial box-model experiments separate the roles of temperature-driven shifts in chemical partitioning, diurnal thermal structure, temperature-dependent isoprene emissions, and humidity. In Shanghai, the increase in O_3 between 30°C and 40°C is dominated by BVOC-driven chemistry, with temperature-amplified isoprene emissions explaining most of the observed response. In Lishui, O_3 sensitivity is governed primarily by radical-NO_x chemistry and thermal PAN-NO_x cycling, with a much smaller role for BVOCs. Fixed RH scenarios substantially reduce the apparent contribution of "thermal chemistry", highlighting humidity-dependent Ox loss and HOx-NOx cycling as key modifiers of the climate penalty. These regime-specific O_3-temperature mechanisms, including BVOC-driven in the urban core, radical-NOx-PAN-driven in the rural area, and significant humidity modulation, provide a process basis for heat-resilient emission controls and demonstrate the value of observation-constrained box models as a bridge to regional chemistry-climate simulations.

1 Introduction

Surface ozone (O_3) remains a prominent air-quality and public-health concern, and its variability reflects a tight coupling between meteorology (temperature, humidity, stability, radiation, etc.) and precursor emissions, with co-occurring heat and O_3 extremes documented (Bloomer et al., 2010; Wang et al., 2022a). As heat extremes, e.g., heatwaves (HWs), increase in frequency, duration, and intensity under continued warming (World Meteorological Organization, 2023), quantifying how O_3 responds to hot conditions is becoming increasingly critical for policymakers (Ebi et al., 2021). In China, summertime O_3 has

https://doi.org/10.5194/egusphere-2026-836
Preprint. Discussion started: 12 March 2026

remained elevated despite recent controls on nitrogen oxides (NO_x = NO + NO_2), underscoring the need to diagnose the meteorological and chemical drivers of O_3 during hot periods (Wang et al., 2022b).

Ozone is a significant air pollutant that adversely affects human health, particularly respiratory functions. Exposure to elevated O_3 concentrations has been linked to increasing rates of respiratory diseases, including asthma and other pulmonary disorders (Cohen et al., 2017; Pope et al., 2023). The Global Burden of Disease Study (Forouzanfar et al., 2015) estimated that in 2015 alone, approximately 254,000 fatalities were attributed to O_3 exposure worldwide, with about 55,300 to 80,300 of those deaths occurring in China (Cohen et al., 2017; Liu et al., 2018). The impacts extend beyond human health: high O_3 levels impair plant physiological processes, detrimentally affect crop yields, and hinder biomass accumulation, thereby threatening food security and ecosystem stability (Meehl et al., 2018; Meng et al., 2023). Moreover, O_3 is also a significant greenhouse gas that further enhances surface warming (Szopa et al., 2021), with positive feedbacks on O_3 levels (Meng et al., 2023).

The underlying relationship between high temperatures and the resultant increase in surface O_3 concentration can be modulated by four primary mechanisms: (i) emissions of O_3 precursors (VOCs), (ii) rates of chemical reaction, (iii) transport and entrainment from the free troposphere, and (iv) deposition of O_3 and its precursors. The meteorological conditions associated with high-temperature events are the key mediators in each pathway and provide the causal links between temperature and the surface O_3 response.

(i) Emissions. The production and destruction of O_3 are highly dependent on its precursors, particularly NO_x and volatile organic compounds (VOCs) (Liu et al., 2021b; Solberg et al., 2008). Biogenic VOC (BVOC) emissions, especially isoprene (C_5H_8), increase exponentially with leaf temperature and light intensity, amplifying O_3 formation under warm, sunny conditions (Chen et al., 2022; Ma et al., 2022a). In addition to BVOC emissions, temperature-dependent evaporative anthropogenic VOC (AVOC) sources, such as petrochemical processing, solvents, and vehicles, will also increase with temperature and have a significant impact in urban environments (Wu et al., 2024; Yamada, 2013).

(ii) Chemistry. Higher temperatures impacts net photochemical processing in the NO_x-hydrogen oxides (HO_x = OH + HO_2)-VOC system by changing rate coefficients and, together with enhanced actinic flux under persistent clear skies, increase photolysis rates; the shift in the radical budget generally results in a net production of O_3, although the reaction rates of several important processes are negatively corelating with increasing temperature (Archibald et al., 2020a; Gu et al., 2020). Thermal decomposition of peroxyacyl nitrate (PAN) type reservoirs (e.g., $CH_3C(O)OONO_2$ (PAN) → $CH_3C(O)OO•$ (PA) + NO_2) at high temperature further shifts reactive nitrogen toward NO_x, favouring O_3 production under NO_x-limited conditions characteristic of rural settings (Steiner et al., 2010; Wu et al., 2008). In addition, low humidity at high-temperature conditions reduces the impact of the reaction $O(^1D)+H_2O \rightarrow 2OH$, thus favouring net O_3 production (Li et al., 2021).

https://doi.org/10.5194/egusphere-2026-836
Preprint. Discussion started: 12 March 2026

(iii) Transport. High-temperature extremes, e.g., heatwaves, frequently coincide with synoptic stagnation, weak circulation and ventilation, and a deeper planetary boundary layer (PBL) (Archibald et al., 2020a; Duc et al., 2022; Utembe et al., 2018; Wu et al., 2019). Stagnation and weak ventilation consistently concentrate O_3 and its precursors, reducing dilution and export, thereby strengthening near-surface accumulation during hot periods (Zhang et al., 2018). On the other hand, a deeper boundary layer at high temperatures generally enhances the ventilation of surface O_3, thereby making it harder for ground-level O_3 to build up (Pfister et al., 2014). The impact of a deeper boundary layer ventilation at high temperatures is partly offset by O_3 entrained from the residual layer aloft (Bloomer et al., 2010).

(iv) Deposition. The deposition velocity (V_d) of O_3 and its precursors is often parameterised as $V_d = (R_a + R_b + R_c)^{-1}$, which represents O_3 deposition as a function of an aerodynamic resistance (R_a), a quasi-laminar boundary layer resistance (R_b), and overall canopy resistance (R_c; stomatal + cuticular + soil) (Stella et al., 2011; Zhang et al., 2003). Here, R_a represents turbulent transport above the canopy (mainly affected by wind speed and stability), R_b describes a quasi-laminar boundary layer resistance for vegetation that depends on the diffusion coefficient of species, and R_c is the surface resistance, combining stomatal, cuticular and soil resistances (Clifton et al., 2020a; Wesely, 1989). During high-temperature extremes, synoptic stagnation and weak near-surface winds reduce turbulent transport near the surface, increasing R_a and R_b resistances and thereby lowering deposition velocity (Wesely, 1989; Zhang et al., 2003). Under hot and dry conditions, high vapour pressure deficit (VPD) and depleted soil moisture reduce stomatal conductance, so the stomatal part of R_c increases, lowering V_d for stomata-controlled species (O_3, NO_2) (Kavassalis and Murphy, 2017; Wilson et al., 2022). Concurrently, hot/dry leaves have minimal surface water films, which raises cuticular resistance and further increases R_c (Clifton et al., 2020a). In contrast, dry soils tend to exhibit lower soil resistance than moist soils, so soil/litter uptake of O_3 strengthens as surfaces dry—partly offsetting the stomatal signal. (Clifton et al., 2020b; Stella et al., 2011).

Complicating this picture are spatial variations in precursor-sensitivity regimes. In NO_x-limited (VOC-rich) environments—typically found in rural and regions downwind of ozone precursor emissions—O_3 production increases nearly linearly with NO_x concentrations and shows limited sensitivity to further VOC additions (Steiner et al., 2006; Utembe et al., 2018). Conversely, in highly urbanised areas with high NO_x/VOC ratios (VOC-limited regime), additional NO_x (mainly emitted in the form of NO) can suppress O_3 by titrating ozone back to NO_2 ($O_3 + NO \rightarrow NO_2 + O_2$), and O_3 formation becomes more strongly driven by available VOCs (Simon et al., 2015). The existence of two regimes implies that identical temperature-driven chemical and meteorological forcings can yield contrasting O_3 responses if background pollutant levels differ, such as in urban versus rural settings, highlighting the need to assess urban-rural differences explicitly.

Most observation-based studies indicated a positive correlation between temperature and tropospheric O_3 levels as a result of the combined effects of O_3's temperature responses, while some found a non-monotonic relationship between temperature and climate penalty factor (O_3-temperature slope, $\Delta O_3/\Delta T$) when ambient temperature exceeds a threshold (Kalisa et al., 2018;

https://doi.org/10.5194/egusphere-2026-836
Preprint. Discussion started: 12 March 2026

Nguyen et al., 2022; Ning et al., 2022; Pusede et al., 2015; Shen et al., 2016; Steiner et al., 2010). Unravelling this complexity requires a careful distinction of how temperature interacts with various atmospheric factors, including solar radiation, humidity, planetary boundary layer height (PBLH), wind speed, precipitation, and both anthropogenic and biogenic emissions (Bloomer et al., 2010; Nguyen et al., 2022; Sun et al., 2017; Wang et al., 2022a; Wu et al., 2008).

Despite the growing body of work on O_3-temperature coupling, significant gaps remain. Observation-constrained box models treat each site as a well-mixed air parcel, apply detailed chemical mechanisms to diagnose local photochemical production and loss rates, provide adjustable environmental parameters, and help separate local chemical controls from transport influences, and are therefore a useful complement to 3-D chemical transport models in studies of extremes (McDuffie et al., 2016). However, few studies have combined observations with process-level box-model budget analyses to quantify the relative contributions of chemical kinetics and precursor changes under extreme-heat conditions. Besides, urban-rural contrasts in O_3 temperature sensitivity have not been systematically explored using consistent methodological frameworks. This is particularly true for rapidly urbanising regions of East Asia, where emission patterns and warming trends interact to shape local O_3 dynamics.

In this study, we investigate the mechanisms of surface O_3's chemical response to high temperatures in contrasting urban and rural environments within the Yangtze River Delta (YRD) region—a hotspot of O_3 pollution in China (Gu et al., 2020; Ma et al., 2022a). Focusing on the summer of 2022 as one example of a summer with significant heatwaves affecting the YRD, we employ a box chemistry model to simulate O_3 production and loss budgets across a temperature range of 25-40 °C. We complement this with a UKESM-AMIP simulation to benchmark the box-derived O_3 chemical production and loss against 3-D diagnostics and to quantify the contribution of omitted physical transport/export to the O_3 budget. Observational input for Shanghai (a VOC-limited regime) and Lishui (a NO_x-limited regime) is drawn from ground-based monitoring networks and emission inventories for June-August. We conduct sensitivity experiments to isolate the impacts of (1) chemical-kinetic temperature dependence, (2) the dependence of the chemistry on humidity, and (3) temperature dependence of BVOC (isoprene) emissions. To define the role of temperature variability, we included two diurnal thermal structures: a realistic diurnal temperature cycle and an extreme condition in which the temperature is held at the daily maximum. By quantifying O_3 production, chemical loss, and deposition of ozone and precursors, we elucidate the divergent temperature sensitivities in urban versus rural contexts.

https://doi.org/10.5194/egusphere-2026-836
Preprint. Discussion started: 12 March 2026

2 Data and Methods

2.1 Study Locations and Observations

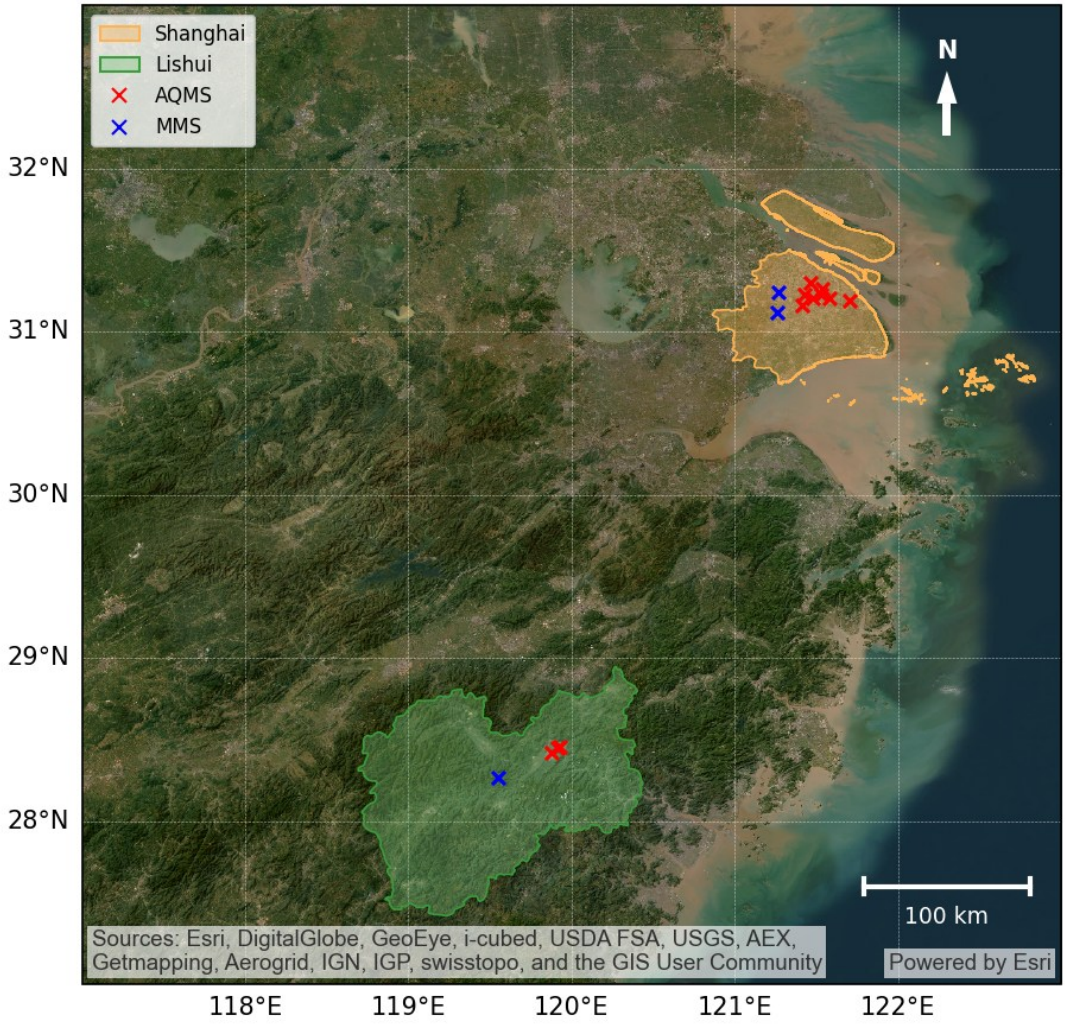

Figure 1. Satellite map of the study domain showing monitoring networks in the Yangtze River Delta. Orange area: Shanghai regional boundary; green area: Lishui regional boundary. Red cross marks: air-quality monitoring stations (AQMS) providing surface O_3 measurements; blue cross marks: meteorological monitoring sites (MMS) providing temperature (T) and relative humidity (RH). The positions correspond to the stations described in Table 1; only sites reporting hourly data for ≥75% of June to August (JJA) 2022 are shown. Basemap: Esri World Imagery (Sources: Esri, DigitalGlobe, GeoEye, i-cubed, USDA FSA, USGS, AEX, Getmapping, Aerogrid, IGN, IGP, swisstopo, and the GIS User Community). Administrative boundaries from the GADM database (www.gadm.org).

https://doi.org/10.5194/egusphere-2026-836
Preprint. Discussion started: 12 March 2026

There are many ways to differentiate between urban and rural environments. Typically, urban and rural areas differ in the types of pollution, emission sources, land use types, plant cover, etc. In ozone-formation chemistry, the chemical regimes determined by ozone precursors are also widely used criteria (Sillman, 1999).

In this study, the Shanghai (SH) and Lishui (LS) regions (orange and green areas, respectively, in Fig. 1) were selected as representative urban and rural environments in eastern China, respectively, with marked differences in local photochemical regimes, population density, and land-use type.

The O_3 precursor regimes were distinguished in subsequent box model simulations: SH in the VOC-limited regime and LS in the NO_x-limited regime (see Section 3.2). As far as population density and land-use type are concerned, Shanghai is a megacity with a population density of 3,900/km^2 (Shanghai Municipal Statistics Bureau, 2024), and construction land covered 42.4% of its total area (Gong et al., 2022). Lishui is an area where 81.7% of the land is covered with forest (Tang et al., 2022). The population density of Lishui is 140/km^2, and the urban district accounts for about 8.6% of its total area (Lishui Municipal Statistics Bureau, 2025).

We collected ground-level hourly O_3 observation data from the China National Environmental Monitoring Center (CNEMC). The AQMSs are in the busiest areas of Shanghai (30.67°N-31.88°N, 120.85°E-122.2°E) and in the populated centre area of Lishui (27.44°N-28.78°N, 118.70°E-120.41°E). Although the Lishui AQMSs are not in a rural setting, they have rural surroundings relatively nearby.

We assessed O_3 and meteorological data for June-August 2022 (JJA 2022) and retained monitoring sites with ≥75% hourly observations during that period. Eight AQMSs and two MMSs in Shanghai, and three AQMSs and one MMS in Lishui met this criterion (spatial distribution see Fig. 1). For each retained site, we extracted hourly surface O_3 and then formed two aggregated series: an urban mean (average across the 8 Shanghai sites at each hour) and a rural mean (average across the 3 Lishui sites at each hour). Meteorological observations originate from the China Meteorological Monitoring System (CMMS) stations; we accessed the archived data via the NOAA National Climatic Data Center (NCDC). The XJH site (Shanghai; 31.12°N, 121.26°E) reports hourly air temperature and dew-point temperature. The BS site (Shanghai; 31.24° N, 121.27° E) and the LS site (Lishui; 28.27° N, 119.55° E) provide three-hourly records of air temperature and dew-point temperature.

https://doi.org/10.5194/egusphere-2026-836
Preprint. Discussion started: 12 March 2026

Table 1. Information on the MMSs (XJH, BS, and LS) and AQMSs in SH and LS

Site code	Full name	Coordinates (°N, °E)	Area	Environment	Variables	Temporal resolution	Period used
XJH	Xujiahui	31.12, 121.26	Shanghai	Urban	Temperature & Dew-point temperature	1h	Jun–Aug 2022
BS	Baoshan	31.24, 121.27	Shanghai	Urban	Temperature & Dew-point temperature	3h	Jun–Aug 2022
LS	Lishui	28.27, 119.55	Lishui	Rural	Temperature & Dew-point temperature	3h	Jun–Aug 2022
1142A	Shiwuchang	31.20, 121.48	Shanghai	Urban	O_3	1h	Jun–Aug 2022
1143A	Hongkou	31.30, 121.47	Shanghai	Urban	O_3	1h	Jun–Aug 2022
1144A	Xuhui Shangshida	31.17, 121.41	Shanghai	Urban	O_3	1h	Jun–Aug 2022
1145A	Yangpu Sipiao	31.27, 121.54	Shanghai	Urban	O_3	1h	Jun–Aug 2022
1147A	Jing'an Station	31.23, 121.43	Shanghai	Urban	O_3	1h	Jun–Aug 2022
1148A	Pudong Chuansha	31.19, 121.70	Shanghai	Urban	O_3	1h	Jun–Aug 2022
1149A	Pudong Xinqu Station	31.23, 121.53	Shanghai	Urban	O_3	1h	Jun–Aug 2022
1150A	Pudong Zhangjiang	31.21, 121.58	Shanghai	Urban	O_3	1h	Jun–Aug 2022
1267A	Jiancezhan Dalou	28.45, 119.91	Lishui	Urban/Suburban	O_3	1h	Jun–Aug 2022
1268A	Dandu Primary School	28.46, 119.93	Lishui	Urban/Suburban	O_3	1h	Jun–Aug 2022
1269A	Yuzhuang Qian	28.42, 119.88	Lishui	Urban/Suburban	O_3	1h	Jun–Aug 2022

The AQMSs in Lishui (1267A-1269A; Table 1) are in a populated area, the environment of which should be regarded as urban or suburban. Nevertheless, the Lishui emission inputs used in the box model (explained in Section 2.2) represent regional mean conditions dominated by low-NOx, biogenically influenced emissions. The resulting chemical regime therefore characterises the regional photochemical environment influencing the city, rather than the immediate urban atmosphere.

https://doi.org/10.5194/egusphere-2026-836
Preprint. Discussion started: 12 March 2026

In this study, a heatwave is defined as a period of at least 3 consecutive days during which the daily maximum temperature exceeds the 90th percentile of the reference period (2000-2019), as used by Zhao et al. (2019). The 90th percentile threshold has been widely used in studies examining heatwave patterns, health impacts, and interactions with air quality (Engdaw et al., 2022; Fischer and Schär, 2010; Sun et al., 2020). To remove day-to-day variation, a 15-day smoothing window centred on the investigated day was applied to threshold calculation (based on the reference period) (García-Martínez and Bollasina, 2021). The years 2020 and 2021 were excluded from the analysis to eliminate any effects resulting from the COVID-19 lockdowns in China.

For the ozone-temperature analysis, we use daily maximum surface O_3 (O_{3max})and daily maximum air temperature (T_{max}) because climate-penalty assessments are conventionally based on daily peak metrics (e.g. daily max 1-h O_3 versus daily T_{max}), which target the photochemical period, reduce confounding nocturnal NO-titration and inter-site timing offsets (Nolte et al., 2021; Otero et al., 2021). We stratify by environment type (urban Shanghai vs. rural Lishui) and by period (all JJA days vs. heatwave days), thus yielding four subsets of ozone-temperature analysis: urban-all, urban-HW, rural-all, and rural-HW.

Daily maximum air temperature values at sites XJH and BS were averaged to obtain the representative Shanghai temperature conditions. To evaluate the joint influence of surface air temperature and humidity on ground-level O_3, we aligned the temporal resolution by applying a 3-hour mean to the hourly O_3 series, ensuring that O_3, temperature, and humidity share the same 3-hourly meteorological sampling times.

2.2 Model configurations and inputs

We use the United Kingdom Chemistry and Aerosols (UKCA) Box Model (equivalent to the Unified Model (UM) version 13.0), which executes the identical UKCA chemistry-aerosol code used in the Met Office UM over a single grid cell (1.25° × 1.9°; zero-D), run independently of the UM. The UKCA Box Model, like other box models, treats each site as a well-mixed air parcel, provides adjustable environmental parameters, and helps separate the contributions of local chemical controls (McDuffie et al., 2016). The box model, by design, does not include advection, convection, and diffusion, enabling fast simulations with direct code-level traceability to UM-UKCA/UK Earth System Model (UKESM) (UKCA, 2025).

Compared to the full 3-D UM-UKCA (e.g. UKESM-AMIP), the box model isolates local chemical-microphysical responses to prescribed forcings (temperature, humidity, photolysis) without transport processes, and completes controlled perturbation experiments orders of magnitude faster, while retaining the StratTrop chemical mechanism used in UKESM1 (Archibald et al., 2020b; UKCA, 2025).

https://doi.org/10.5194/egusphere-2026-836
Preprint. Discussion started: 12 March 2026

The aim of the UKCA Box model simulation in this study is to build two contrasting chemical environments: an urban case dominated by anthropogenic transport/industrial emissions (Shanghai-like chemical environment) and a rural case dominated by biogenic VOC emissions (Lishui-like chemical environment). The highly controllable climate forcing enables attribution of the O_3 temperature response to (1) chemical-kinetic temperature dependence, (2) the dependence of the chemistry on humidity, (3) temperature dependence of BVOC (isoprene) emissions, and (4) diurnal temperature structure. A 3-D UKESM-AMIP simulation was performed to benchmark the box against a fully resolved chemistry-meteorology system, providing grid-cell-mean O_3 production and loss diagnostics under the same chemistry scheme and quantifying the budget contributions absent from the box configuration, particularly transport/export. To ensure comparability and avoid ambiguity arising from administrative-area differences between Shanghai and Lishui, O_3 budget calculations were carried out by configuring the box to match the UM grid size (1.25° × 1.9°). Box-model emissions were initialised from CEDS by averaging a small set of CEDS cells adjacent to the corresponding UM grid cells (Fig. 2) and were then tuned to satisfy observed precursor constraints; this preserves an inventory-consistent baseline while yielding urban/rural chemical environments that remain comparable to the UKESM grid-cell context (Table 3).

In the box model simulations in this study, photolysis varies diurnally with the solar-zenith angle at the target latitude/longitude. At the same time, meteorological and surface parameters are consistent with YRD summer-average values unless noted. Temperature and relative humidity are set in each experiment as described in Table 2 (see Section 2.3).

We repeat a representative summer-day radiation cycle until the system attains a steady state (defined as a state in which the variation in the output daily mean values of key chemical species is within ±0.1% of the previous day). To avoid analysing relatively unimportant partitioning between O_3 and closely related odd-oxygen species, we focus our analysis on the wider odd-oxygen family (Ox) (using UKCA definition as $O_x = O_3 + O(^1D) + O(^3P) + NO_2 + 2NO_3 + 3N_2O_5 + HNO_4 + HNO_3 +$ PANs) were used as output indicators here (Bates and Jacob, 2020; Hu et al., 2017). The model time resolution is 10 minutes. Initial trace-gas fields follow the standard ST_urban UKCA box initial-condition set, while the initial concentrations of key O_3 precursors are tuned with observations where available (See Supplement).

https://doi.org/10.5194/egusphere-2026-836
Preprint. Discussion started: 12 March 2026

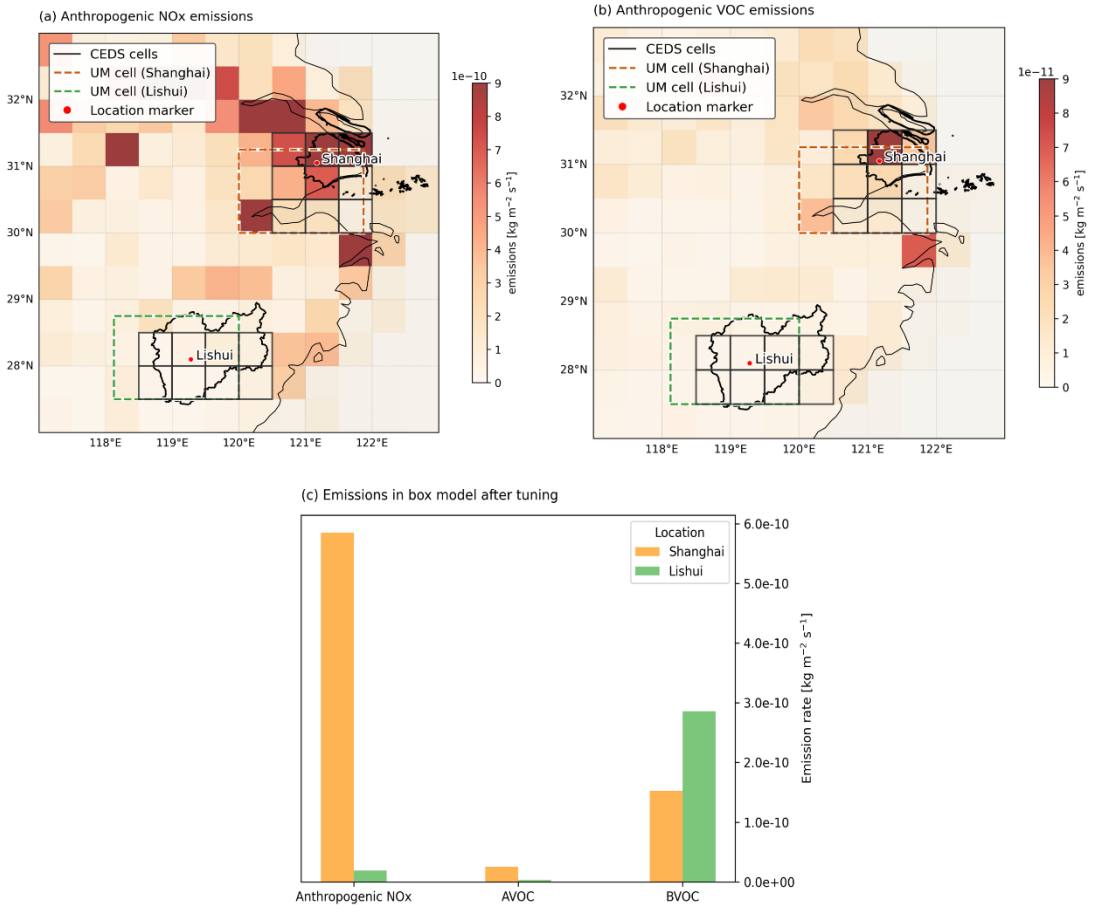

Figure 2. Anthropogenic and biogenic emission fields and their aggregation for the model set-up. (a) Community Earth atmospheric Data System (CEDS; accessed at https://github.com/JGCRI/CEDS) anthropogenic NO_x emissions over the study region (colour scale in kg NO m^{-2} s^{-1}). (b) CEDS AVOC emissions (colour scale in kg VOC m^{-2} s^{-1}; VOC emissions were added up of C_2H_6, C_3H_8, and HCHO emissions, selection criteria see Supplement). (a,b) Spatial selection used to define the Shanghai and Lishui model emissions: municipal outlines (black); CEDS grid cells included in each background (grey squares); and the corresponding UKCA/UM single grid cell used for the box model (dashed outline; orange for Shanghai, green for Lishui). (c) Emissions applied in the box model for each location—anthropogenic NOx, AVOC, and BVOC—after averaging the emissions in selected cells shown in panel (a,b) and tuned (tuning method see Supplement) (units: kg m^{-2} s^{-1}). Emissions were aggregated as the arithmetic mean over the selected CEDS cells (9 cells for Shanghai; 8 cells for Lishui), chosen to be close to the UM cell while covering the main municipal area. Offshore islands are included only where they fall within the selected CEDS cells. Coastlines from Natural Earth (naturalearthdata.com). Administrative boundaries from the GADM database (www.gadm.org).

https://doi.org/10.5194/egusphere-2026-836
Preprint. Discussion started: 12 March 2026

We included emission and deposition fluxes in the box model. The anthropogenic emissions were based on grid inventory data from the CEDS for the 2022 JJA summer period. CEDS cells adjacent to the UM cells were selected (as shown in Figure 2a, 2b) to ensure the box simulations were as comparable as possible with UKESM simulations. Biogenic VOC emissions were taken from the China inventory of Wu et al. (2020), estimated using the MEGAN v2.1 framework (Guenther et al., 2012). Deposition of relevant compounds was also included, specifically O_x species, CO, and HCHO, based on the parameterisation of deposition fluxes in the UKCA model which represents deposition processes as described by Wesely (1989).

Due to coarse CEDS emission grid cells and the absence of physical transport mechanisms in the UKCA Box Model, emission and deposition values from data sources can cause deviations in gas species levels from local observations. To ensure the box model simulations are representative of local conditions, local O_3 emissions and depositions were tuned to maintain daily mean O_3 and key precursors (CO, HCHO, C_5H_8 and/or NO_2, depending on observation availability and representativeness; see Supplement Table 1) outputs within ±30% of the observed values at baseline conditions. The baseline conditions were set to average local humidity and temperatures for JJA 2022, with the diurnal temperature cycle and the temperature dependence of isoprene disabled (Ori experiment settings, 30 °C, 70% RH, Pressure = 100 kPa, and PBLH = 590 m). In this process, the depositions in the UKCA Box model were designed to be representative of both physical transport and deposition and were tuned primarily. The emission values used in the Box model are shown in Fig. 2(c).

A full 3-D UKCA model simulation reproducing the 2022 summer was conducted and compared with the Box model simulations. This simulation was performed using the UKESM-AMIP setup with the UM version 13.3. The model was run with a horizontal resolution of 1.25° by 1.9° (as shown on Fig. 2) with 85 vertical levels up to 85 km (Walters et al., 2019), and the GLOMAP-mode aerosol scheme, which simulates sulfate, sea salt, BC, organic matter, and dust but does not simulate nitrate aerosol (Mulcahy et al., 2020). The chemistry scheme used was Strat-Trop (Archibald et al., 2020b), identical to the box model. Anthropogenic and biomass burning emissions were from the SSP3-7.0 scenario from the CEDS (shown in Fig.2), as described by Hoesly et al. (2018). Oceanic emissions were from the POET 1990 data set (Olivier et al., 2003), and all biogenic emissions except isoprene and monoterpenes were based on 2001-2010 climatologies from the Model of Emissions of Gases and Aerosols from Nature under the Monitoring Atmospheric Composition and Climate project (MEGAN-MACC) version 2.1 (Guenther et al., 2012). Isoprene and monoterpene emissions were generated interactively using the iBVOC parameterisation and were shown in Fig. 2c (Pacifico et al., 2011).

Temperature and horizontal wind fields were nudged (Telford et al., 2013) in the model run to the ECMWF ERA5 reanalyses for 2022 from ECMWF (Dee et al., 2011) to constrain the atmospheric conditions as close to the observations as possible. Nudging only occurred above ~1200 m in altitude to avoid surface effects, and thus, the majority of the planetary boundary layer was not nudged.

https://doi.org/10.5194/egusphere-2026-836
Preprint. Discussion started: 12 March 2026

A 6-month run from March 1 2022, to August 31 2022, was conducted with the nudged UKESM-AMIP model. In the UKESM-AMIP input environment settings, monthly sea surface temperature (SST) and sea ice concentration (SIC) under the SSP2-4.5 scenario were used. The first three months are considered the model spin-up. The output of the nudged UKESM-AMIP simulation was provided as monthly mean values, while the grid cells for Shanghai and Lishui were chosen as in Fig. 2.

285

2.3 Sensitivity experiments

Table 2. Sensitivity experiments of the UKCA Box Model (VRH = fixed absolute humidity (=RH 70% at 30C); FRH = variable absolute humidity (=RH 70%))

Index	Experiment	RH	Diurnal cycle (D)	T-dependent isoprene emission (ft)	Environmental background
	Shanghai – Variable RH (VRH)				**Urban**
1	SH_VRH_Ori	Change with T	No	No	Urban
2	SH_VRH_D	Change with T	Yes	No	Urban
3	SH_VRH_ft	Change with T	No	Yes	Urban
4	SH_VRH_Dft	Change with T	Yes	Yes	Urban
	Lishui – Variable RH (VRH)				**Rural**
5	LS_VRH_Ori	Change with T	No	No	Rural
6	LS_VRH_D	Change with T	Yes	No	Rural
7	LS_VRH_ft	Change with T	No	Yes	Rural
8	LS_VRH_Dft	Change with T	Yes	Yes	Rural
	Shanghai – Fixed RH (RH = 70%)				**Urban**
9	SH_FRH_Ori	Fixed at 70%	No	No	Urban
10	SH_FRH_D	Fixed at 70%	Yes	No	Urban
11	SH_FRH_ft	Fixed at 70%	No	Yes	Urban
12	SH_FRH_Dft	Fixed at 70%	Yes	Yes	Urban
	Lishui – Fixed RH (RH = 70%)				**Rural**
13	LS_FRH_Ori	Fixed at 70%	No	No	Rural
14	LS_FRH_D	Fixed at 70%	Yes	No	Rural
15	LS_FRH_ft	Fixed at 70%	No	Yes	Rural
16	LS_FRH_Dft	Fixed at 70%	Yes	Yes	Rural

https://doi.org/10.5194/egusphere-2026-836
Preprint. Discussion started: 12 March 2026

We conducted a set of 16 sensitivity experiments (Table 2) with the UKCA Box Model to isolate the effects of temperature, humidity, diurnal temperature variation, and temperature-dependent isoprene emissions on near-surface O_3. Each of the experiments was further conducted seven times to explore the influence of environmental temperature, which spanned the range 25-40 °C at 2.5 °C increments, while keeping all the other settings fixed according to the experiment name. These follow the naming convention <location>_<RH>_<process>:

- Location: SH = Shanghai, urban background; LS = Lishui, rural background.
- RH setting: VRH = relative humidity varying with temperature, fixed absolute humidity (=RH 70% at 30 °C); FRH = relative humidity fixed at 70 %, variable absolute humidity (see Appendix Table S2).
- Process: D = diurnal cycle in air temperature enabled; ft = temperature-dependent isoprene emission factor ft enabled; Dft = both enabled; Ori = both disabled

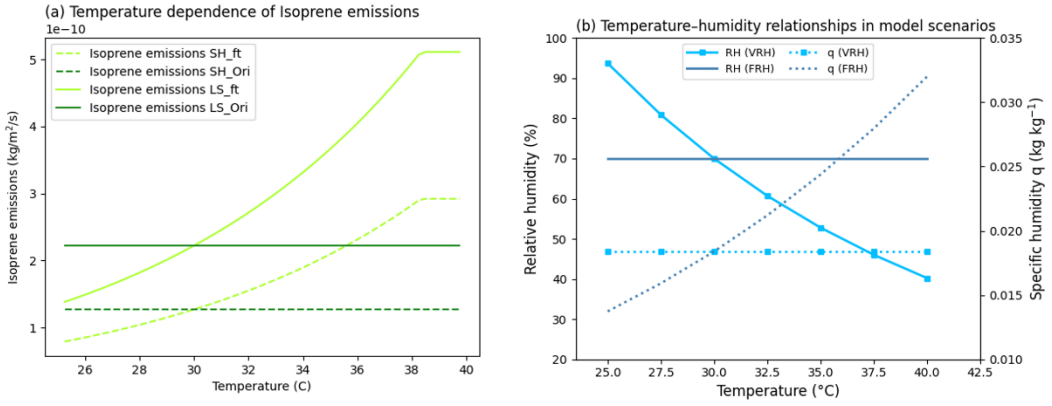

Figure 3. Model settings for the isoprene temperature dependence and the humidity scenarios. (a) Isoprene emission response to temperature used in the sensitivity configurations. Solid lines (LS) and dashed lines (SH) show cases with the temperature-dependent factor ft enabled (_ft) versus the baseline with ft disabled (_Ori, isoprene emissions constant with baseline conditions). The ft response increases with T and saturates at 38.3 °C; emission rates are shown in kg m^{-2} d^{-1} (left axis). (b) Two humidity scenarios respond to temperatures in humidity settings. The VRH case (lines with markers) applies temperature-dependent RH and constant q, while the FRH case (lines) holds constant RH and temperature-dependent q. Axes show RH (%) on the left and q (kg kg^{-1}) on the right.

Two binary switches modify the model processes: D and ft. D (diurnal temperature enabled) applies a realistic diurnal cycle to the target-temperature (daily maximum) day; when D is off, air temperature is held constant at the target value, an extreme

https://doi.org/10.5194/egusphere-2026-836
Preprint. Discussion started: 12 March 2026

condition in which daily minimum values equal daily maximum values. The temperature-dependent isoprene emission factor ft enables the temperature response of isoprene.

The temperature response of isoprene followed the equations below:

$$isoprene\ emissions = \ local\ summer\ average\ emissions * ft$$

The ft is the isoprene temperature dependence factor (Pacifico et al., 2011):

$$ft = e^{0.1*(T-30)}\ when\ e^{0.1*(T-30)} < 2.3\ (T\ in\ °C)$$
$$ft = 2.3 \qquad when\ e^{0.1*(T-30)} \geq 2.3\ (T\ in\ °C)$$

Where T is temperature in centigrade.

In these experiments, isoprene emissions increase with temperature until they reach their plateau at 38.3 ℃ (as shown in Figure 3); when ft is off, isoprene emissions are temperature-independent.

The reference conditions were set at 30 °C and 70% RH (mass mixing ratio of water (q) = 0.0184 kg/kg), representing the average environmental conditions in the 2022 JJA summer in the YRD based on observed values. Unless stated otherwise, pressure and boundary-layer height are held at the baseline values (Pressure = 100 kPa, PBLH = 590 m), which are the averaged YRD summer conditions based on observations and ECMWF ERA5 reanalyses in 2022. Photolysis varies diurnally with the solar zenith angle at the site's latitude/longitude, so it shows a sinusoidal variation peaking at midday and being zero at night. The clouds were ignored, and all simulations are under clear-sky conditions. The location settings determine initial species levels.

https://doi.org/10.5194/egusphere-2026-836
Preprint. Discussion started: 12 March 2026

3 Results

3.1 Observed O_3 response to temperature and humidity variations

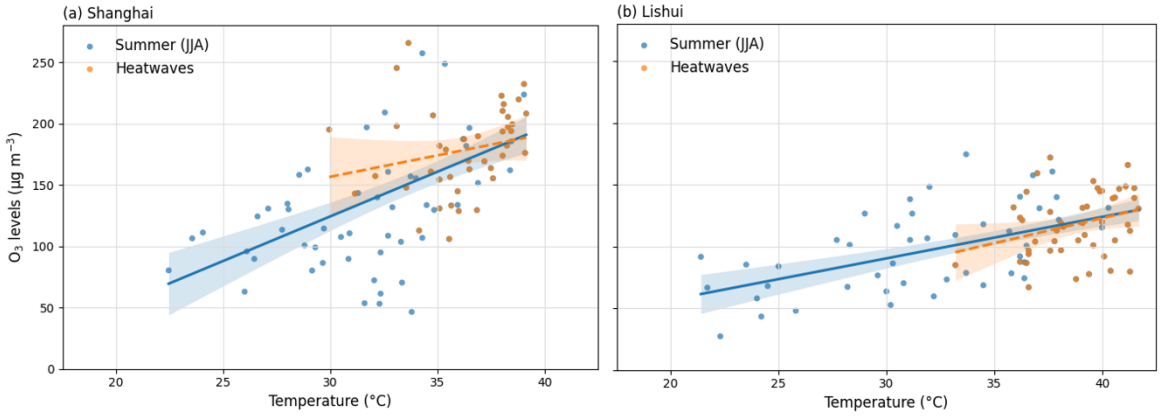

Figure 4. Relationship between observed daily maximum surface ozone concentration and air temperature (based on hourly data) during the summer 2022 (JJA; blue) and heatwave days (orange; definition see Section 2.1) for (a) Shanghai and (b) Lishui. Points are the daily maximum values (average values for sites; spatial distribution shown in Figure 1); solid (JJA) and dashed (heatwave) lines are ordinary-least-squares fits. Shaded envelopes show the 95% confidence intervals for the fitted lines.

Figure 4 depicts the relationship between daily maximum surface ozone and daily maximum temperature for summer 2022, shown for Shanghai and Lishui during all JJA days and just HW days. Across both data subsets (JJA and HW days), and at both locations (Shanghai and Lishui), O_{3max} increases with T_{max}, resulting in positive correlations. Averaged over eight Shanghai sites, the summertime O_3 fractional change per unit temperature change is 7.27 μg m^{-3} $°C^{-1}$ with a 95 % confidence interval (CI) [5.13, 9.41] and $p < 0.01$. The corresponding mean sensitivity across three Lishui sites is 3.36 μg m^{-3} $°C^{-1}$ (95 % CI [2.30, 4.41], $p < 0.01$).

This urban-rural contrast is consistent with differences in the chemical regime. As reported by Gu et al. (2020), Shanghai exhibits a strong VOC-limited regime in O_3 formation, where temperature increases enhance BVOC emissions while NO_x remains abundant, leading to a relatively strong ozone-temperature relationship. By contrast, the rural areas in YRD generally show higher VOC abundance, and the effect of temperature is less pronounced than in VOC-limited areas because BVOC changes here have a negligible impact (Jin and Holloway, 2015). Those differences in chemical regimes are also supported by model simulation results in this study (Sect. 3.2; Fig. 6). Thus, the doubled O_3 sensitivity to temperature in Shanghai compared

https://doi.org/10.5194/egusphere-2026-836
Preprint. Discussion started: 12 March 2026

to Lishui is consistent with stronger NO_x availability and generally higher pollution levels in Shanghai, and may relate to the capacity for PAN thermal decomposition in the YRD (detailed PAN analysis see Fig. 10) (Steiner et al., 2010).

Regressions during HWs indicate a different behaviour at the two locations. In Lishui, the heatwave-period O_{3max}-T_{max} sensitivity is 4.05 μg m^{-3} $°C^{-1}$ (95% CI [0.203, 7.899], $p < 0.05$), indicating a significant positive association between O_{3max} and T_{max} during HW periods. By contrast, in Shanghai, the Ordinary Least Squares (OLS) slope estimated from heatwave days is 3.49 μg m^{-3} $°C^{-1}$ with 95% CI [−1.464, 8.441] ($p = 0.16$, $n = 41$), so a statistically significant linear association is not supported. The range of 95% CI includes zero, indicating substantial uncertainty in the direction and magnitude of ozone's temperature response during the 2022 summer heatwaves in Shanghai. Including more historical heatwave data may help diagnose whether this loss of significance is due to insufficient data or suggest that additional heatwave co-factors (e.g., stagnation, humidity, precursor variability, or chemical regime shifts) could modulate the O_3-T linkage in Shanghai.

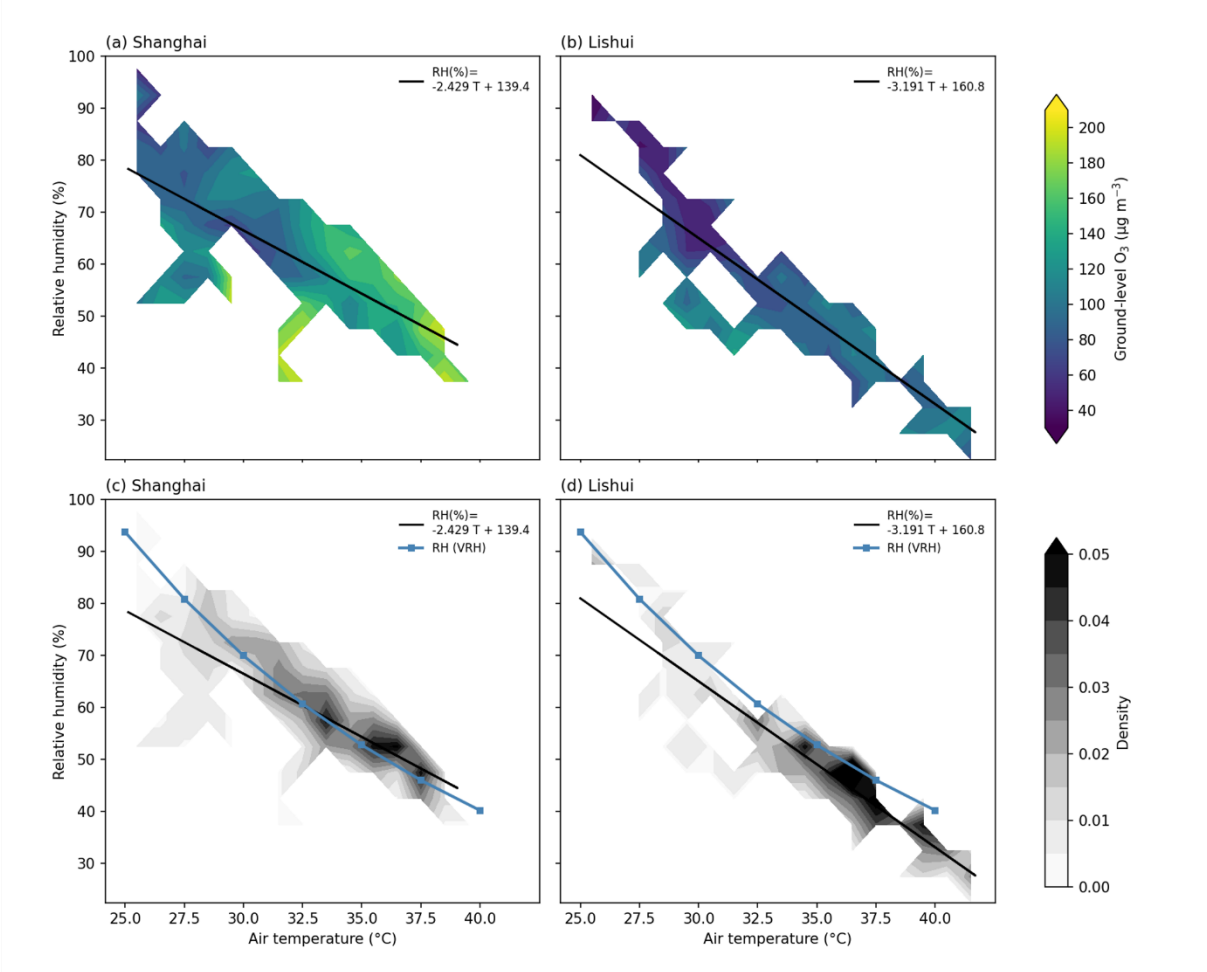

https://doi.org/10.5194/egusphere-2026-836
Preprint. Discussion started: 12 March 2026

Figure 5. Observed air temperature-relative humidity space for (a, c) Shanghai and (b, d) Lishui (daytime, T ≥ 25 °C), Panels (a-b) show the ground-level O_3 (μg m^{-3}) binned on a 1 °C × 5 % RH grid; panels (c-d) show the data density (fraction of site samples per bin) on the same grid. The solid black line in each panel is the ordinary-least-squares fit of RH to T from the unbinned 3-hourly records. Ozone: hourly observations averaged from 8 AQMS (Shanghai) and 3 AQMS (Lishui); meteorology: three-hourly MMS data; all aggregated to 3-h means. The blue solid line with square markers in panels (c-d) is the RH curve with conserved absolute humidity (q=0.0184 kg kg^{-1}) used in the VRH model scenario.

Figure 5 summarises how daytime ground-level O_3 varies with T and RH in Shanghai and Lishui. In both regions, RH decreases systematically with warming. In Shanghai, the typical RH spread within a given temperature bin is about 20 % (e.g. 45-65 % at 35 °C), with larger variability at lower T and progressively narrower ranges at higher T (Fig. 5c). Lishui shows a similar tendency, with most samples concentrated between 32-37 °C and 35-55 % RH (Fig. 5d). Across the observed T-RH space, O_3 increases with temperature and decreases with RH, indicating a preference for warm, dry conditions.

Linear regression of RH on T yields slopes of −2.429 % $°C^{-1}$ for Shanghai and −3.191 % $°C^{-1}$ for Lishui ($p < 0.01$ in both cases). The weaker slope in Shanghai, together with its narrower T range, is consistent with the moderating influence of sea-land thermal and moisture exchanges on coastal boundary-layer conditions, whereas the steeper slope in Lishui reflects a greater propensity for hot-dry excursions in a forested inland setting. The RH-T co-variation is much tighter in Shanghai (R^2 = 0.83) than in Lishui (R^2 = 0.57): in Shanghai the highest-density region (Fig. 5c) and the strongest O_3 increases (Fig. 5a) lie close to the regression line, implying that the linear T-RH relationship provides a good description of typical warm-season daytime conditions and of the pathway along which O_3 responds to combined warming and drying. In Lishui, by contrast, the main density maximum lies above the regression line and does not coincide with the dominant O_3-increase pathway, indicating that the fitted slope is influenced by a smaller number of hot, anomalously dry episodes. This behaviour is consistent with previous studies reporting that Lishui RH conditions are dominated by strong evapotranspiration from vegetation and soils, which is negatively correlated with temperature over the YRD in summer (Wang et al., 2023). In addition, stomatal closure under low-humidity conditions, which always corresponds to high-temperature conditions, would reduce O_3 dry deposition and further enhance O_3 levels (Kavassalis and Murphy, 2017), contributing to the high-O_3 tail at the hot, dry end of the Lishui distribution.

In Figs. 5c and 5d, we compare relative humidity from the VRH model configuration used in the subsequent simulations—defined by a conserved absolute humidity equal to the regional JJA 2022 mean (q = 0.0184 kg kg^{-1})—with the observed T-RH distribution. The VRH curve follows the locus of highest observational density in both Shanghai and Lishui, indicating that this configuration provides a realistic representation of the humidity-temperature conditions sampled in 2022 and is therefore suitable as the baseline humidity scenario for the box-model experiments.

https://doi.org/10.5194/egusphere-2026-836
Preprint. Discussion started: 12 March 2026

Overall, Figure 5 demonstrates that hot, dry conditions are favourable for elevated O_3 at both sites, but that the joint T-RH-O_3 variability differs between the coastal megacity and the forest-surrounded inland region: Shanghai exhibits a stronger, more coherent O_3-T-RH relationship in summer 2022 than Lishui, reflecting differences in local meteorology, surface characteristics, precursor emissions and chemical regime.

To interpret these observed O_3-temperature-humidity relationships in terms of process contributions and mechanisms, we next use an observation-constrained box model to quantify the extent to which the observed high-temperature O_3 response can be explained by changes in local chemical kinetics, precursor abundances, temperature diurnal cycles, and humidity conditions. Furthermore, the mechanisms underlying process contributions will be explored through budget-level simulations.

3.2 Evaluation of the Box Model performance

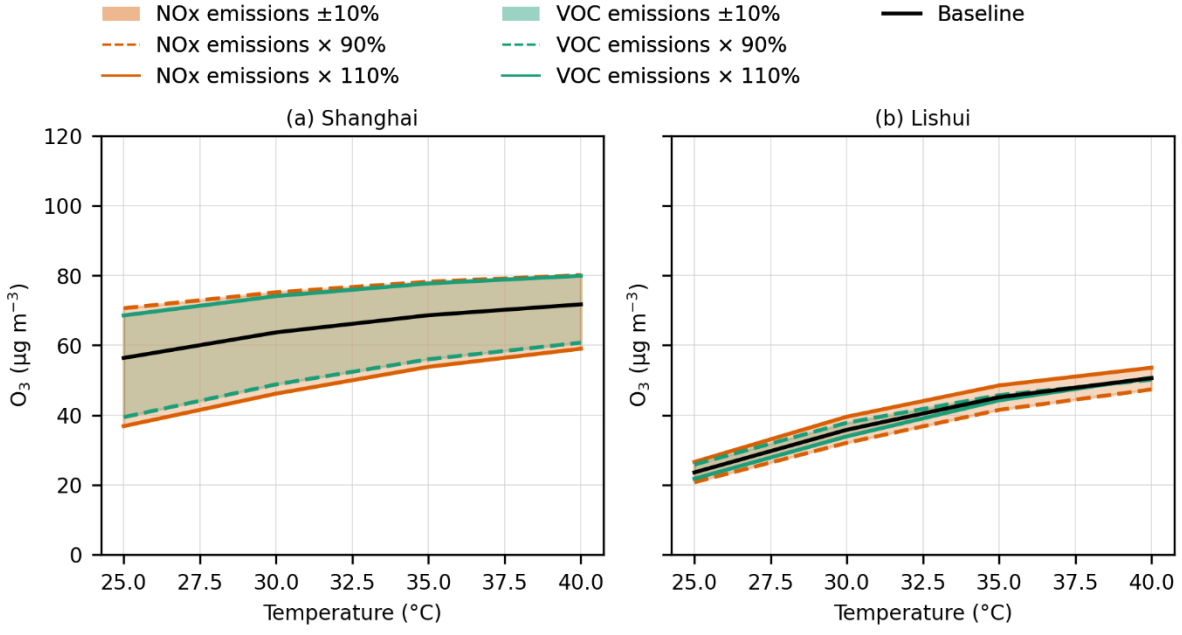

Figure 6. Simulated responses of daily mean surface O_3 to ±10 % perturbations in NO_x and VOC emissions under consistent chemical-meteorological conditions in the UKCA Box Model based on VRH_Ori settings. Experiments were performed at 25, 30, 35, and 40 °C. Shaded areas denote the O_3 ranges between reduced (× 90%) and enhanced (× 110%) emissions for NO_x (orange) and VOCs (green). Solid and dashed lines show individual perturbation cases, and the black line indicates the baseline simulation (emissions × 1.0).

Figure 6 summarises the box-model sensitivity experiments used to diagnose precursor regimes in Shanghai (Fig. 6a) and Lishui (Fig. 6b). For the baseline experiment, where there are no other processes but chemical reaction rates and pathways

https://doi.org/10.5194/egusphere-2026-836
Preprint. Discussion started: 12 March 2026

changing with temperature (marked as Ori), surface O_3 levels show a moderate response to temperature in both Shanghai and Lishui area. The daily mean O_3 increment from 25 to 40 °C in Shanghai is 15.3 μg m^{-3}, whereas it is 27.0 μg m^{-3} in Lishui. At 30 °C and 70 % RH, the baseline simulations are broadly consistent with the observed conditions in the 28.75-31.25 °C temperature bin. In Shanghai, the daily-mean O_3 is 63.7 μg m^{-3} in the model versus 69.5 μg m^{-3} in the observations. In Lishui, the corresponding values are 35.8 μg m^{-3} (model) and 52.5 μg m^{-3} (observations), a low bias that is consistent with Lishui being NO_x-limited (see below) and suggests that the grid-cell-average NO_x levels in the box configuration are lower than those sampled by the monitoring site. Further details of the simulated O_3-T relationships and their comparison with observations are discussed in Sect. 3.3.

In Shanghai (Fig. 6a), O_3 decreases with higher NO_x emissions and increases with higher VOC emissions, indicating a VOC-limited regime (Pusede et al., 2015). The O_3 reduction under NO_x enhancement reflects the dominance of radical termination via OH + NO_2 reactions and the associated suppression of HO_x recycling. Conversely, increasing VOCs elevates O_3 through enhanced peroxy-radical (RO_2) production and faster propagation cycles. The absolute magnitudes of the O_3 response for VOC and NO_x perturbations are similar, implying a substantial photochemical leverage of VOC availability and NOx abundance on local O_3 formation. This VOC-limited behaviour is consistent with the high-NO_x, anthropogenically dominated environment of Shanghai and agrees with Liu et al. (2021b)'s study on the effectiveness of emission control strategies in China's major urban areas.

In contrast, Lishui (Fig. 6b) exhibits the opposite tendency: O_3 increases with NO_x enhancement and is only weakly affected by VOC perturbations, signifying a NO_x-limited regime (Utembe et al., 2018). The positive O_3 response to additional NO_x suggests that peroxy-radical (HO_2/RO_2) concentrations exceed those required for efficient O_3 formation, such that O_3 production is constrained by oxidant initiation rather than termination. The small VOC sensitivity implies that biogenic precursors already provide sufficient radical sources under summertime conditions. This behaviour is characteristic of rural or suburban photochemical environments influenced by regional BVOC emissions and relatively low NO_x levels (Sillman, 1999). The contrasting regimes between the two regions underscore the distinct emission structures and radical chemistry operating within the YRD. While Shanghai's O_3 formation is primarily controlled by anthropogenic VOC abundance and thus sensitive to solvent- and transport-related emissions, Lishui's O_3 depends more on NO_x inputs from surrounding regions and long-range transport (Li et al., 2019). The similar temperature dependence across all cases further indicates that temperature-dependent chemical effects of reaction rates amplifies but does not fundamentally alter the chemical regime classification in those box model simulations. Overall, those experiments confirm that the photochemical environment in Shanghai is VOC-limited, whereas Lishui resides in a NO_x-limited regime—providing a mechanistic foundation for the O_3-temperature slopes and O_x budgets discussion in the following section.

https://doi.org/10.5194/egusphere-2026-836
Preprint. Discussion started: 12 March 2026

Table 3. Comparison of PAN, OH, HO_2, and C_5H_8 levels in observation, UKCA Box Model, and UKESM-AMIP

Species	Location	Environment	Year	Period	Value type	Value (ug/m3)	Source type	Reference
PAN	Shanghai	Urban	2017	Summer	Hourly maximum	4.4	Observation	Zhang et al. (2021)
	Shanghai	Urban	2022	Summer	Daily mean	7.1	UKCA Box	This study
	Shanghai	Urban	2022	Summer	Daily mean	3.9	UKESM	This study
	Nanjing	Background	2020	Summer	Daily mean	2	Observation	Xu et al. (2024)
	Hangzhou	Suburban	2021	Summer	Daily mean	6.7	Observation	Wu et al. (2023)
	Lishui	Rural	2022	Summer	Daily mean	3.6	UKCA Box	This study
	Lishui	Rural	2022	Summer	Daily mean	3.5	UKESM	This study
OH	Shanghai	Urban	2019	Nov–Dec	Noon mean (11:00-13:00)	7.6 * 10-5	Observation	Zhang et al. (2022)
	Shanghai	Urban	2022	Summer	Daily mean	1.0 * 10-4	UKCA Box	This study
	Shanghai	Urban	2022	Summer	Daily mean	9.4 * 10-4	UKESM	This study
	Taizhou	Suburban	2018	May–Jun	Daily maximum	3.0 * 10-4	Observation	Ma et al. (2022)
	Lishui	Rural	2022	Summer	Daily mean	1.4 * 10-5	UKCA Box	This study
	Lishui	Rural	2022	Summer	Daily mean	5.2 * 10-5	UKESM	This study
HO2	Shanghai	Urban	2019	Nov–Dec	Noon mean (11:00-13:00)	4.4 * 10-3	Observation	Zhang et al. (2022)
	Shanghai	Urban	2022	Summer	Daily mean	9.4 * 10-3	UKCA Box	This study
	Shanghai	Urban	2022	Summer	Daily mean	9.8 * 10-2	UKESM	This study
	Taizhou	Suburban	2018	May–Jun	Daily maximum	6.2 * 10-2	Observation	Ma et al. (2022)
	Lishui	Rural	2022	summer	Daily mean	2.9 * 10-2	UKCA Box	This study
	Lishui	Rural	2022	summer	Daily mean	2.1 * 10-2	UKESM	This study
C5H8	Shanghai	Urban	2018	July	Daily mean	0.8	Observation	Gu et al. (2022)
	Shanghai	Urban	2022	summer	Daily mean	0.3	UKCA Box	This study
	Shanghai	Urban	2022	summer	Daily mean	2.4	UKESM	This study
	Lishui	Rural	2009	September	Daytime average	8.3	Observation	Geng et al. (2011)
	Lishui	Rural	2022	summer	Daily mean	6.6	UKCA Box	This study
	Lishui	Rural	2022	summer	Daily mean	6.1	UKESM	This study

Table 3 makes a cross-comparison among several key species in O_3 formation chemistry. For the values in Table 3, observations are collected from recent studies, UKCA Box Model simulations are conducted under baseline conditions (Ori settings, 30 °C, and 70% RH), and the UKESM-AMIP simulation is nudged with ERA5. For the species, PAN determines the thermal responses of NO_x; HO_x is critical in the O_3 photochemical cycle; and C_5H_8 is the major contributor to VOC emissions' temperature responses in summer. Here, PAN, HO_x, and C_5H_8 are chosen as indicators to evaluate how well the UKCA Box Model reproduces the ozone chemical environment in the following temperature-sensitivity experiments.

https://doi.org/10.5194/egusphere-2026-836
Preprint. Discussion started: 12 March 2026

Overall, those species are reasonably close to observations and the nudged UKESM-AMIP simulation. While the PAN and C_5H_8 values can be directly compared across, the values of HO_x would be better described as between the observations and UKSEM-AMIP outputs. We speculate this could be due to differences between point measurements and grid point averages in the model simulations. Additionally, the different emission input grids used in the UKCA Box Model and the UKESM-AMIP model (see Fig. 2) may also cause a mismatch, as HO_x levels are sensitive to O_3 precursor emissions.

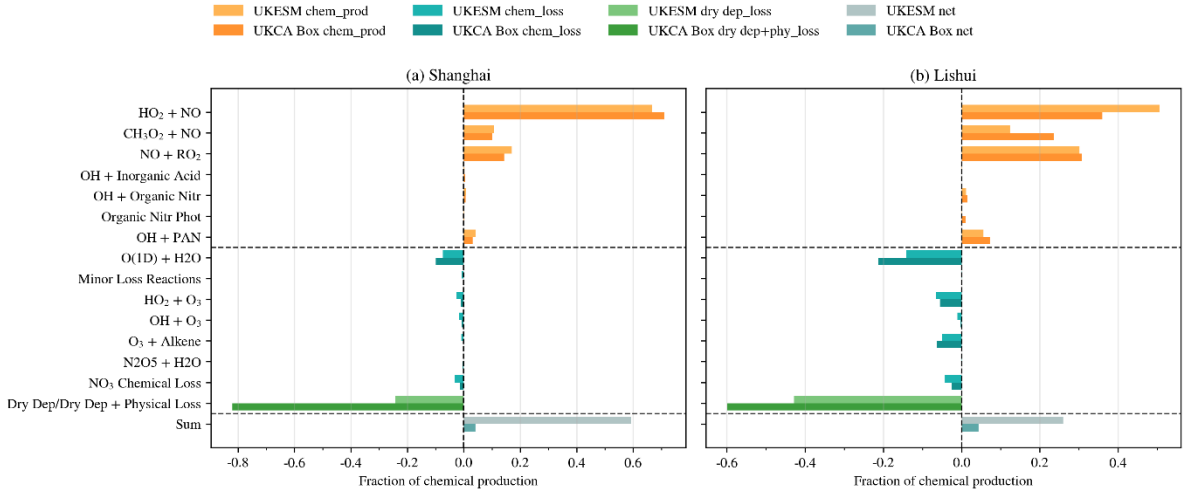

Figure 7. O_x production-loss budget by process category for two models at two sites. Panels (a-b) show the fractional contribution to total chemical production (unitless) from each reaction class. Positive bars denote chemical production (orange tones), negative bars denote chemical loss (teal tones) and dry deposition (UKESM) / dry deposition + physical transport (UKCA Box) loss (green tones); the grey bar at the far right gives the net sum. Darker shades represent UKESM and lighter shades the UKCA Box. Reaction classes on the y-axis include major O_x production and loss pathways. (a) Shanghai; (b) Lishui. Box model simulations were conducted under baseline conditions (Ori settings, 30 °C, and 70% RH). The JJA averaged temperature and humidity in UKESM are 27.1 °C and 71.9% RH.

Figure 7 evaluates how the UKCA Box partitions O_x sources and sinks relative to UKESM at Shanghai (SH) and Lishui (LS). Two complementary diagnostics are shown: the fractional compared to total chemical production (panels a-b).

The Box Model reproduces the rank order of production pathways in the nudged UKSEM-AMIP model. In Shanghai, the total O_x production flux is 1.62×10^{-9} kg m^{-2} s^{-1} in the Box model versus 2.03×10^{-9} kg m^{-2} s^{-1} in the UKESM model. And in Lishui, this O_x production flux is 4.10×10^{-10} kg m^{-2} s^{-1} in the Box model, while this value is 8.40×10^{-10} kg m^{-2} s^{-1} in the UKESM. In both cities, peroxy-NO reactions (HO_2 + NO and RO_2/CH_3O_2 + NO) dominate the chemical production fraction in the box model, matching the pattern in UKESM and consistent with summertime O_3 photochemistry described by Ma et al. (2022b).

https://doi.org/10.5194/egusphere-2026-836
Preprint. Discussion started: 12 March 2026

This agreement in fractional chemistry indicates that the box model captures the regime (NO_x-VOC-OH coupling) rather than simply tuning totals. Chemical loss through $O(^1D) + H_2O \rightarrow 2OH$ and radical-ozone reactions ($HO_2 + O_3$, $OH + O_3$) is represented with similar sign and relative importance in both frameworks.

The UKCA Box simulation shows a larger fractional contribution from dry deposition to the O_x sink (Fig. 5a-b). In the 3-D UKESM simulations, this sink is explicitly divided into deposition and dynamical export (not shown in Fig. 7; dynamical export refers to physical transport and mixing, including horizontal advection, vertical entrainment with the growing boundary layer, shallow/deep convection, and ventilating outflow). In contrast, the box model treats the air parcel as a closed, well-mixed volume with no transport, so all non-chemical removal must appear as a lower-boundary deposition term. According to the monthly mean O_3 levels from June to August (UKESM) and the trend of daily mean O_3 levels (UKCA box model), both UKESM and UKCA Box produce nearly constant surface O_3, indicating that the net O_x tendency is close to zero. In UKESM, this large residual ("UKESM sum") reflects the contribution of dynamical export. In the box model, the production-loss balance is achieved by having chemical production intentionally offset by the parameterised dry-deposition term, leaving only a small net production or loss. The larger deposition fraction in UKCA Box should therefore be interpreted as representing the combined effect of true surface uptake and the export processes, which are explicitly resolved in UKESM.

Taken together, the panels support the view that the UKCA Box model captures the controlling processes of summertime O_x chemistry in the UKESM model at both sites: production dominated by $HO_2/RO_2 + NO$, chemically plausible loss channels, and a reasonable net budget. Remaining differences in absolute magnitudes most likely reflect representativeness and surface parameterisation (deposition velocities, boundary-layer depth) rather than a structural failure of the chemical scheme. For this reason, the current comparison indicates that the box model provides a reliable, site-scale diagnostic of O_x production and loss suitable for interpreting observed O_3 behaviour and precursor control.

https://doi.org/10.5194/egusphere-2026-836
Preprint. Discussion started: 12 March 2026

3.3 Temperature responses of ozone in the box model and observations

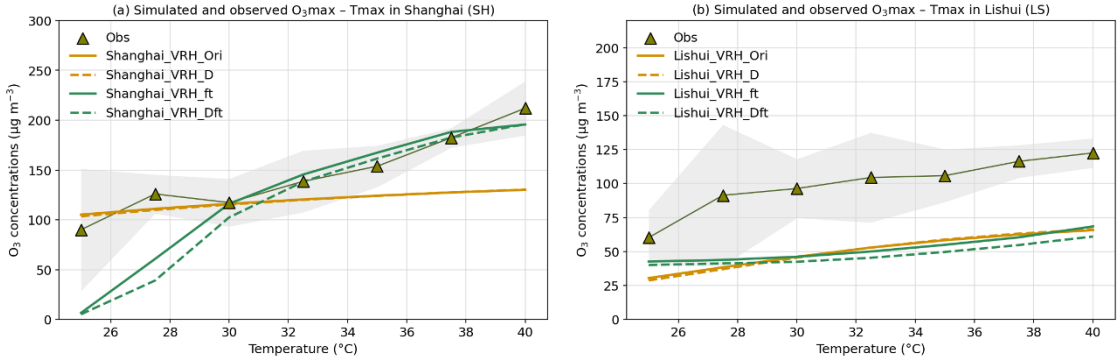

Figure 8. Comparison of observed and simulated O_{3max}-T_{max} relationships for (a) Shanghai and (b) Lishui (summer, JJA). Observations are shown as olive triangles connected by a line; the grey envelope denotes the 95% confidence interval of the observed bin means (2.5 °C T_{max} bins; e.g., the 25 °C bin denotes summer days with T_{max} 23.75-26.25 °C). Colored solid/dashed lines show the four model configurations (VRH_Ori, VRH_D, VRH_ft, VRH_Dft; see Table 2).

Figure 8 compares observed JJA O_{3max}-T_{max} relationships in the VRH set of experiments with the UKCA Box Model: Ori (reference – fixed temperature and isoprene emissions across all hours of day), D (diurnal temperature cycle only), ft (temperature-dependent isoprene only), and Dft (both). The main purpose of these sensitivity experiments is to evaluate the impact of those processes on O_3's temperature responses. In the box model simulations, the VRH experiments exhibit a trend in RH-temperature that resembles reality; thus, these experiments are considered reasonably good evaluators of the box model's performance when compared with observations.

Shanghai (urban; Fig. 8(a)). Above 30 ℃, the ft and Dft simulations exhibit significant coordination in both ozone concentrations and trend, indicating that the temperature dependence of isoprene emissions explains most of the observed sensitivity in this regime. Relative to Ori and D, both ft and Dft lift O_3 by about 20 to 40 μg m^{-3} at 32.5-37.5 °C and reproduce the monotonic increase with temperature. At T < 30 °C, observations align more closely with Ori/D, whereas ft/Dft are low biased. Two factors likely contribute: (i) wider uncertainty at the cool end (grey 95 % CI band) owing to fewer low-temperature days in summer 2022, and (ii) meteorological controls (e.g., mixing depth, advection, cloudiness) that covary with temperature but are not explicitly represented in the box model, which isolates chemical responses. At the upper tail, the simulated slope weakens because the applied isoprene function saturates at ~38.3 °C, reducing the Dft (and ft) response from 9.3 μg m^{-3} $°C^{-1}$ between 35-37.5 °C to 2.1 μg m^{-3} $°C^{-1}$ between 37.5-40 °C; the observations maintain a steeper gradient (≈12 μg m^{-3} $°C^{-1}$). The

https://doi.org/10.5194/egusphere-2026-836
Preprint. Discussion started: 12 March 2026

different isoprene emission threshold might be the cause, since suppression of isoprene emissions was not observed in the 10-40 °C range in Shanghai (Gu et al., 2022). And additional heat-linked processes (e.g., boundary-layer dynamics, anthropogenic VOCs, or NOx variability) may continue to amplify O_3 at extreme temperatures.

Lishui (rural; Fig. 8(b)). The simulations reproduce the shape of the observed O_3-T curve, but the simulated O_3 is systematically low-biased by about 50 μg m^{-3}. This offset is consistent with site representativeness (i.e. the observations exhibit a populated area in Lishui where NO_x emissions are higher than the box model simulations, which cover the whole Lishui region, most of which are rural areas). Importantly, introducing temperature-dependent isoprene (ft/Dft) yields only minor changes relative to Ori/D, indicating that Lishui operates largely in a NO_x-limited regime where additional VOC reactivity produces only modest O_3 increases, i.e. including T-dependence for isoprene leads to higher VOC levels, but this doesn't increase O_3 in Lishui, whereas it does in Shanghai. The small influence of the D option confirms that, after binning by Tmax, imposing a diurnal temperature cycle alone does not substantially alter daily O_{3max} in this case.

Overall, the VRH experiments show that the UKCA Box captures the observed temperature sensitivity of O_3 when the isoprene-temperature coupling is represented (Shanghai), while the weak ft/Dft effect at Lishui is consistent with NO_x limitation. Discrepancies at low temperatures and in the highest bins highlight the role of meteorology and extreme-heat processes that lie outside the box configuration, motivating targeted sensitivity tests (e.g., boundary-layer depth, deposition, NO_x variability) in future work.

Table 4. Changes in daily maximum O_3 (ΔO_{3max}) from 30 to 40 °C

Unit: μg m^{-3}

Scenario	Observation	Ori_FRH	Ori_VRH	D_FRH	D_VRH	ft_FRH	ft_VRH	Dft_FRH	Dft_VRH
ΔO_3 in Shanghai	94.77	14.05	17.75	14.63	18.68	62.02	83.26	74.96	96.83
ΔO_3 in Lishui	26.21	11.66	21.08	13.04	22.4	14.43	23.81	12.43	21.57

Table 4 presents the increase in O_{3max} from 30 to 40 °C for the observations and the box model experiments. Because the experiments differ only in the process switched on, we quantify each process's contribution to the O_3 warming response by comparing the simulated 30 to 40 °C change. For each experiment X, we define $\Delta O_3^X = O_3^X$ (40 °C) − O_3^X (30 °C), and similarly, ΔO_3^{obs} from the observations. All metrics below are expressed as fractions of ΔO_3^{obs} and therefore dimensionless. The net chemical response is $f_{chem} = \Delta O_3^{VRH\_Ori} / \Delta O_3^{obs}$, i.e., the fraction of the observed 30 to 40 °C increase that can be explained by temperature-dependent gas-phase chemistry alone under VRH conditions. The additional effect of each process is then quantified as the incremental fraction of ΔO_3^{obs} gained when that process is switched on: for the diurnal cycle, $f_{diurnal} = (\Delta O_3^{VRH\_D} - \Delta O_3^{VRH\_Ori}) / \Delta O_3^{obs}$; for the isoprene temperature dependence, $f_{iso} = (\Delta O_3^{VRH\_ft} - \Delta O_3^{VRH\_Ori}) / \Delta O_3^{obs}$; and for

https://doi.org/10.5194/egusphere-2026-836
Preprint. Discussion started: 12 March 2026

humidity, f_{humid} = (ΔO_3^{FRH} - ΔO_3^{VRH}) / ΔO_3^{obs}. Positive values indicate that the process amplifies the increase in O_3 with temperature, whereas negative values indicate damping. This normalisation allows us to directly compare the extent to which the observed O_3-temperature sensitivity can be attributed to each process at the two sites.

In Shanghai, decomposition of the Ox budget shows that the net chemical term accounts for 18.7 % of the observed 30 to 40 °C increase, while the diurnal temperature cycle alone has a negligible effect on the net chemistry. By contrast, the temperature dependence of isoprene emissions explains 73.0 % of the observed O_3 rise, identifying this pathway as the dominant driver of the warm-season O_3-T slope in urban Shanghai. When isoprene's temperature sensitivity is enabled, the diurnal cycle yields an additional 14.3 % O_3 increment, consistent with enhanced photolysis and radical propagation during warmer, sunnier hours reported in YRD (Xia et al., 2022).

Humidity acts as an important modulator of the O_3-temperature response. In our experiments, increasing RH by about 30 % at 40 °C (FRH: q=0.0320 kg kg^{-1}, RH = 70%; VRH: q=0.0184 kg kg^{-1}, RH = 40.2%), while keeping the temperature diurnal cycle and isoprene temperature dependence switched on (VRH_Dft settings), leads to a 21.7 μg m^{-3} reduction in O_{3max} at 40 °C. Expressed as a fraction of the observed 30 to 40 °C change, this contribution is ($\Delta O_3^{FRH\_Dft}$ - $\Delta O_3^{VRH\_Dft}$) / ΔO_3^{obs}. This humidity-driven decrease reflects the role of water vapour in enhancing O_x loss via $O(^1D) + H_2O$ pathway: in the FRH case, the vertically integrated $O(^1D) + H_2O$ flux (kg m^{-2} s^{-1}) increases by about 42 %, strengthening the O_3 decomposition pathway and offsetting part of the thermally driven O_3 enhancement.

In the NO_x-limited regime (i.e. Lishui), the process attribution gives different results. The chemical response itself explains 80.4% of the observed 30→40 °C change, implying that enhanced photochemistry at higher temperatures—through faster reaction rates and stronger actinic flux—dominates the O_3 increase (Archibald et al., 2020a). The isoprene temperature dependence contributes only 10.4 %, consistent with a NO_x-limited environment where additional VOC reactivity produces comparatively small changes in O_3 production (Steiner et al., 2006). The diurnal temperature cycle makes only a minor contribution to the 30→40 °C O_3 increase, whereas the humidity perturbation is non-negligible. When RH is raised from 40.2 % to 70 % at 40 °C (VRH: q = 0.0184 kg kg^{-1}; FRH: q = 0.0320 kg kg^{-1}) under the VRH_Dft settings, the resulting change in humidity accounts for 9.1 μg m^{-3} of O_{3max} reduction. O_x budget diagnostics show that this damping arises from two linked effects of higher water vapour: a reduction in O_x production via the HO_2 + NO channel (≈ 15.3 % reduction in FRH scenarios compared with that in VRH scenarios), and an enhancement of O_x loss via O_3 photolysis followed by $O(^1D) + H_2O$ (≈ 36.9 % compared with VRH scenarios). Both mechanisms are consistent with Li et al. (2021), who showed that elevated relative humidity suppresses O_3 generation by inhibiting the OH/HO_2-NO_2 chain and promotes O_3 loss through the $O(^1D) + H_2O$ pathway.

https://doi.org/10.5194/egusphere-2026-836
Preprint. Discussion started: 12 March 2026

595 Taken together, Figure 8 and Table 4 demonstrate that the UKCA Box model produces a physically interpretable decomposition of the O_3-temperature relationship: isoprene-temperature coupling is decisive in Shanghai, while baseline chemical partitioning and humidity dominate in Lishui. These site-specific attributions align with the contrasting chemical regimes and underscore the need to represent both biogenic VOC responses and meteorologically linked processes when projecting O_3 extremes under warming.

600 **3.4 Temperature response on O_x, PAN, and HO_x diurnal cycles**

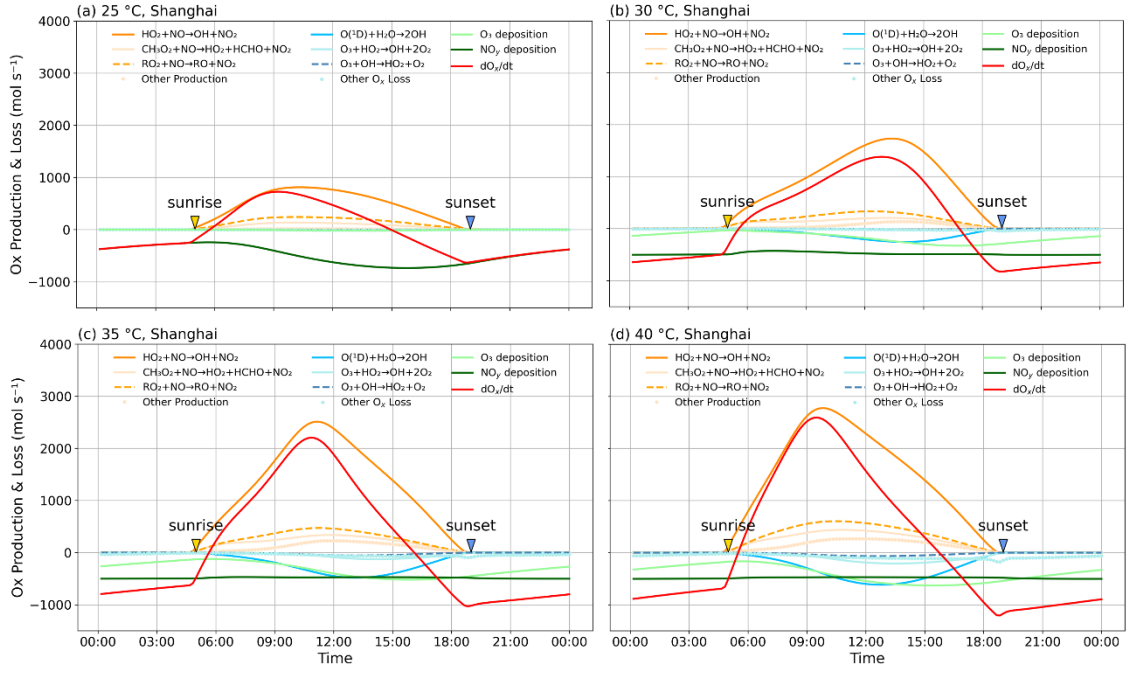

Figure 9(A). Shanghai (Dft configuration): diurnal Ox budget at four simulated Tmax — (a) 25 °C, (b) 30 °C, (c) 35 °C, (d) 40 °C. Curves show major chemical production pathways (orange), chemical loss terms (blue), deposition loss terms (green), and the net tendency dOx/dt (red). Arrows indicate local sunrise and sunset. Axes are shared across panels; units are mol s^{-1};
605 time is local.

https://doi.org/10.5194/egusphere-2026-836
Preprint. Discussion started: 12 March 2026

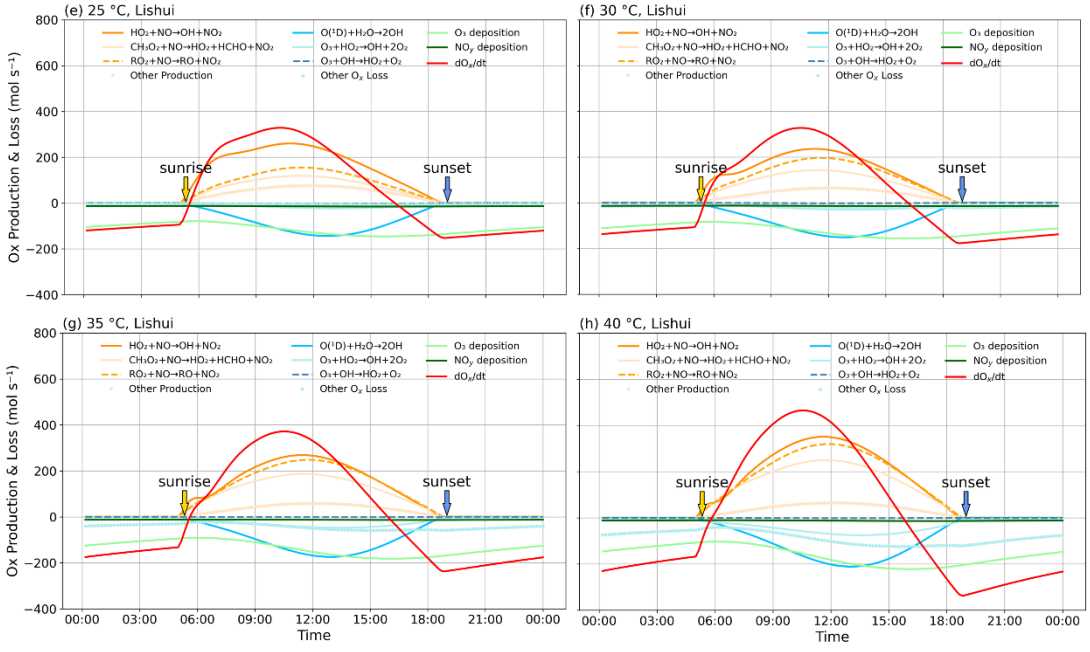

Figure 9(B). Lishui (Dft configuration): same diagnostics as Fig. 9 for (e) 25 °C, (f) 30 °C, (g) 35 °C, (h) 40 °C Tmax simulations.

https://doi.org/10.5194/egusphere-2026-836
Preprint. Discussion started: 12 March 2026

Table 5. O_x budget sensitivity to temperature in urban and rural areas (unit: $tO_x\ day^{-1}$; O_x counted as O_3)

Table 5(a). Daily contribution of main production and loss pathways to the O_x budget at 25, 30, 35, and 40 °C in Shanghai

Unit: tOx day^{-1}

Process \ Temperature (°C)	25	30	35	40
Chemical Production				
HO_2+NO	1150.5	2305.7	3100.6	3559.9
CH_3O_2+NO	193.8	322	489	640.2
RO_2+NO	357.4	476.9	649.1	856.8
OH + INORG ACID	7.6	17.3	28.9	28.4
OH + ORG NITR	9.5	22.9	37.1	57.1
ORG NITR PHOT	4.1	3.2	3.8	5.3
OH + PAN REACT	3.7	96.2	193.8	271.9
Total Chem Prod	**1726.7**	**3244.3**	**4502.3**	**5419.7**
Chemical loss				
$O(^1D)$+H_2O	17.4	292.8	567.5	751.2
MINOR LOSS REACTIONS	11	4.5	4.2	4.8
O_3+HO_2	0	23.2	132.8	256.2
O_3+OH	0.2	19.9	58.7	80.8
O_3 + ALKENE	0.5	5.2	12	26.4
N2O5 + H_2O	0	17.7	41.5	53.6
NO_3 Chemical loss	0.1	32.7	103.9	214.9
Total Chem Loss	**29.3**	**395.9**	**920.7**	**1387.9**
Deposition (& transport) loss				
O_3 dry Deposition	21.8	711.7	1323.3	1688.8
NOy Deposition	2013.7	2006.9	2011.2	2012.5
Total Dep (& trans) Loss	**2035.4**	**2718.5**	**3334.5**	**3701.3**

https://doi.org/10.5194/egusphere-2026-836
Preprint. Discussion started: 12 March 2026

Table 5(b). Daily contribution of main production and loss pathways to the O_x budget at 25, 30, 35, and 40 °C in Lishui

Unit: tOx day^{-1}

Temperature (°C) / Process	25	30	35	40
Chemical Production				
HO_2+NO	380	334.7	371.2	475.5
CH_3O_2+NO	173.4	209.3	275.1	365.9
RO_2+NO	217.8	275.9	348	444.5
OH + INORG ACID	0.1	0	0	0
OH + ORG NITR	9.5	11.6	16.2	25.3
ORG NITR PHOT	3	7.1	14.2	24.3
OH + PAN REACT	99.9	74.5	53.1	42.5
Total Chem Prod	**883.7**	**913.2**	**1077.8**	**1377.9**
Chemical loss				
$O(^1D)$+H_2O	187.8	196.6	224.8	269.3
MINOR LOSS REACTIONS	0	0.1	0.1	0.1
O_3+HO_2	35.6	48.3	74.5	117.2
O_3+OH	4	2	1.6	1.9
O_3 + ALKENE	11.7	46.9	132.7	267.8
N2O5 + H_2O	0.1	0	0	0
NO_3 Chemical loss	6.5	15.9	35.8	69.5
Total Chem Loss	**245.8**	**309.6**	**469.6**	**725.8**
Deposition (& transport) loss				
O_3 dry Deposition	470.7	496.7	564.9	669.5
NOy Deposition	56.2	54.1	52.2	49.3
Total Dep (& trans) Loss	**526.9**	**550.8**	**617.1**	**718.8**

https://doi.org/10.5194/egusphere-2026-836
Preprint. Discussion started: 12 March 2026

Figure 9 and Table 5 summarise how O_x production and loss terms from the UKCA Box Model respond to temperature. In Shanghai (Fig. 9a-d; Table 5a), all major production pathways increase with temperature, except for organic-nitrate photolysis (labelled ORG NITR PHOT in Table 5a), which has a minor impact on total production. From Fig. 9a-d, the reaction HO_2 + NO → OH + NO_2 is the dominant and most temperature-sensitive source of O_x production. Although its marginal sensitivity (change in Ox production per °C) weakens from 25→40 °C, it remains the single largest contributor. The second key source, RO_2 + NO → RO + NO_2, displays the opposite behaviour—its temperature sensitivity strengthens with warming. From 35 to 40 °C, the contribution of RO_2 + NO to total O_x production increases by 207.7 tOx day^{-1} in Shanghai, nearly doubling the increase from 25 to 30 °C, underscoring the growing role of peroxy-radical chemistry at high temperatures. This growth is consistent with high-temperature partitioning of the OH-HO_2-RO_2 cycle—most notably the HO_2+NO channel—and with the well-documented increase in effective VOC reactivity under hot conditions due to both faster kinetics and temperature-sensitive VOC emissions (e.g. isoprene) (Meng et al., 2023). Even with reduced temperature sensitivity, the HO_2 + NO reaction accounted for 50.1 % of total chemical production, confirming the importance of the HO_2-NO pathway in the urban regime.

For chemical loss in Shanghai, $O(^1D)$ + H_2O → 2OH is the leading term. Its temperature sensitivity is 55.01 tO_x day^{-1} $°C^{-1}$ between 25-35 °C, decreasing to ~36.74 tO_x day^{-1} $°C^{-1}$ from 35-40 °C, consistent with partial saturation of midday photolysis at the hottest conditions. In the total budget, however, deposition dominates loss. O_3 dry deposition exhibits the stronger temperature sensitivity—maximising between 30-35 °C—whereas NO_y deposition varies less with temperature but remains the largest absolute sink at all temperatures, controlling the sign of the net O_x tendency. As deposition in the UKCA Box Model serves both as deposition and as physical loss, the magnitude comparison is not so useful.

In Lishui (Fig. 9e-h; Table 5b), both production and loss magnitudes are substantially smaller than in Shanghai, consistent with lower precursor loadings in rural southwestern Zhejiang and the prevalence of NO_x-limited chemistry outside urban cores in the YRD (An et al., 2021; Ren et al., 2022). HO_2 + NO is still the largest single production term, but at T > 30 °C its strength becomes comparable to CH_3O_2 + NO and RO_2 + NO, indicating a more distributed peroxy-NO contribution in the regional background. For chemical loss, $O(^1D)$ + H_2O dominates from 25-30 °C. At temperatures higher than 30 °C, O_3 + ALKENE reactions' contribution grows rapidly with temperature and becomes comparable in magnitude to $O(^1D)$ + H_2O, highlighting the role of thermally enhanced VOC-ozone chemistry outside the urban core where the O_3 + C_5H_8 reaction plays a crucial role. In the depositional budget, O_3 dry deposition is relatively more important in Lishui than in Shanghai, consistent with the much larger vegetated land fraction—which elevates deposition velocity of O_3 via stomatal and surface uptake—and with weaker in-situ NO_y production under rural low-NO_x conditions (Clifton et al., 2020b).

Overall, the Box model yields a coherent, process-level explanation for the observed O_3-temperature behaviour. In Shanghai, warming amplifies O_x primarily through HO_2 + NO chemistry while deposition—especially NO_y deposition—limits the net build-up. In Lishui, the warming response is shared more evenly among peroxy-NO sources, and O_3 deposition plays a larger role in the sink, with O_3-alkene loss emerging at the hottest conditions.

https://doi.org/10.5194/egusphere-2026-836
Preprint. Discussion started: 12 March 2026

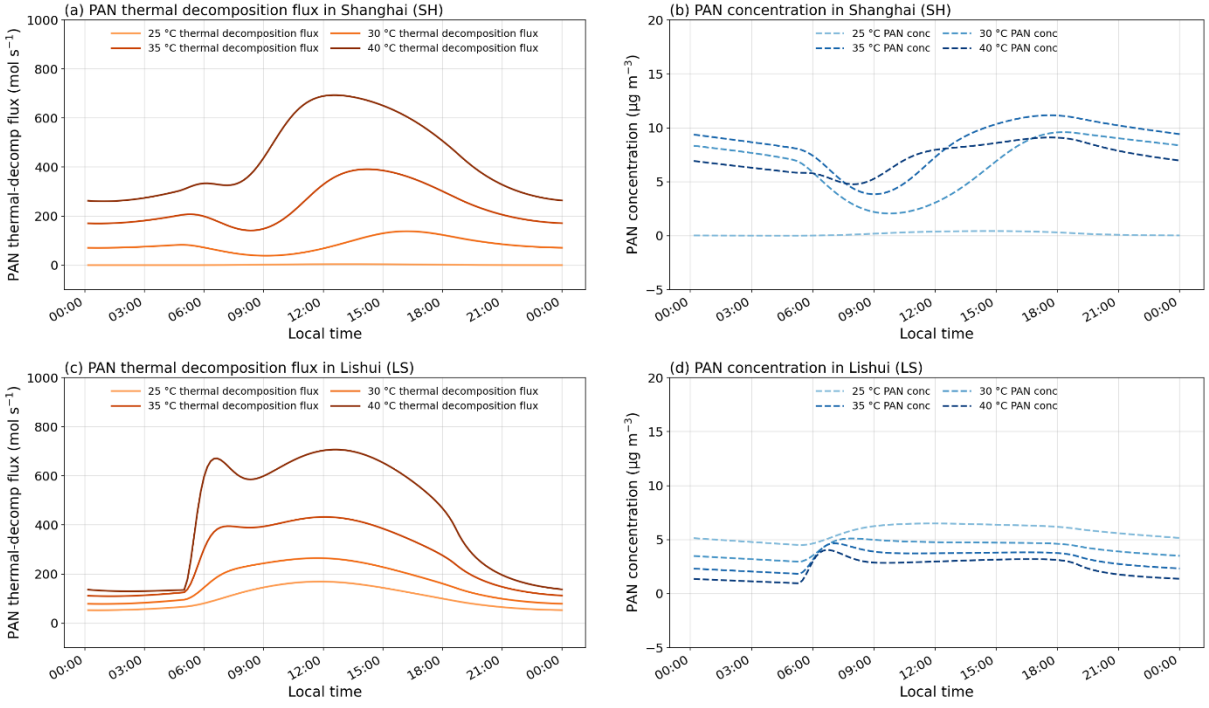

Figure 10. Diurnal peroxyacetyl nitrate (PAN) budget at four temperatures. Panels (a-b) Shanghai and (c-d) Lishui. Solid orange curves show the PAN thermal-decomposition flux (left axis, mol s^{-1}); dashed blue curves show PAN concentration (right axis, μg m^{-3}). Each pair corresponds to a temperature scenario (25, 30, 35, 40 °C; lighter→darker with increasing temperature). Local time on the x-axis.

Figure 10 contrasts the diurnal evolution of peroxyacetyl nitrate (PAN) concentrations (dashed curves, right axis) with the thermal decomposition flux PAN → $CH_3C(O)O_2$ (PA) + NO_2 (solid curves, left axis) at four imposed temperatures in Shanghai (panel a) and Lishui (panel b). In both locations, the decomposition flux increases monotonically with temperature and peaks around local noon-early afternoon, with daytime values far exceeding nighttime values. This behaviour is consistent with the strong temperature dependence of the PAN stability (PAN thermally decomposes rapidly at higher temperatures) and with daytime heating that accelerates the decomposition reaction (Fischer et al., 2014).

Despite the broadly similar flux patterns, concentration responses differ by site. In Lishui (Fig. 10c-d), PAN concentrations decrease with warming across the full range. As the temperature rises, thermal loss outpaces daytime production (due to low ambient NO_x), so the reservoir is progressively depleted. The result is a clean negative PAN-T relationship.

https://doi.org/10.5194/egusphere-2026-836
Preprint. Discussion started: 12 March 2026

In Shanghai, the response is non-monotonic. In Fig. 10b, from 25 to 35 °C, the PAN concentration increases, even as the thermal decomposition of PAN accelerates as shown in Fig. 10a. This implies that, over this range, enhanced PAN production—via larger peroxyacetyl radical supply and abundant NO_2—offsets the faster loss, allowing concentrations to rise. However, at 40 °C, the pattern reverses after midday: the decomposition flux jumps sharply relative to 35 °C, while the PAN concentration drops in the afternoon. Two explanations, which are not mutually exclusive, are consistent with the curves. First, PAN's thermal instability means the PA+NO_2⇌PAN equilibrium shifts strongly toward PAN dissociation at high temperature (Cleary et al., 2007); thermal loss is the primary PAN sink in the lower troposphere and accelerates through the warmest hours, producing the observed afternoon drawdown in Fig. 10a. Second, extreme heat coincides with lower afternoon PAN production efficiency, e.g. due to the reduction in biogenic precursor supply, e.g., C_5H_8 as an indirect source of PA encountered its threshold at 38.3 °C, or enhanced radical competition (Liu et al., 2021a; Ma et al., 2022a; Phillips et al., 2013), so low peroxyacetyl radical (PA) levels limit the reaction between PA + NO_2 to form PAN. This PAN concentration drop may imply a threshold of PAN thermal decomposition above 40 °C in Shanghai, which occurs above 39 °C in California as described by Steiner et al. (2010).

A further notable contrast is the lower temperature behaviour (25 °C). Both the thermal decomposition flux and the PAN concentration are lower in Shanghai than in Lishui at this temperature, indicating that, under cooler conditions, PAN acts as a less effective NO_x reservoir near the urban site.

Overall, Figure 10 shows that warming consistently strengthens PAN thermal decomposition at both sites, but the net concentration response is site-specific: monotonic decreases in Lishui, and increases followed by depletion in Shanghai at the highest temperature. These distinctions have practical implications: during heat extremes, PAN-mediated transport of NO_x is likely reduced because rapid afternoon decomposition limits PAN lifetime in VOC-limited urban areas like Shanghai, and the effect can be less significant in Lishui.

https://doi.org/10.5194/egusphere-2026-836
Preprint. Discussion started: 12 March 2026

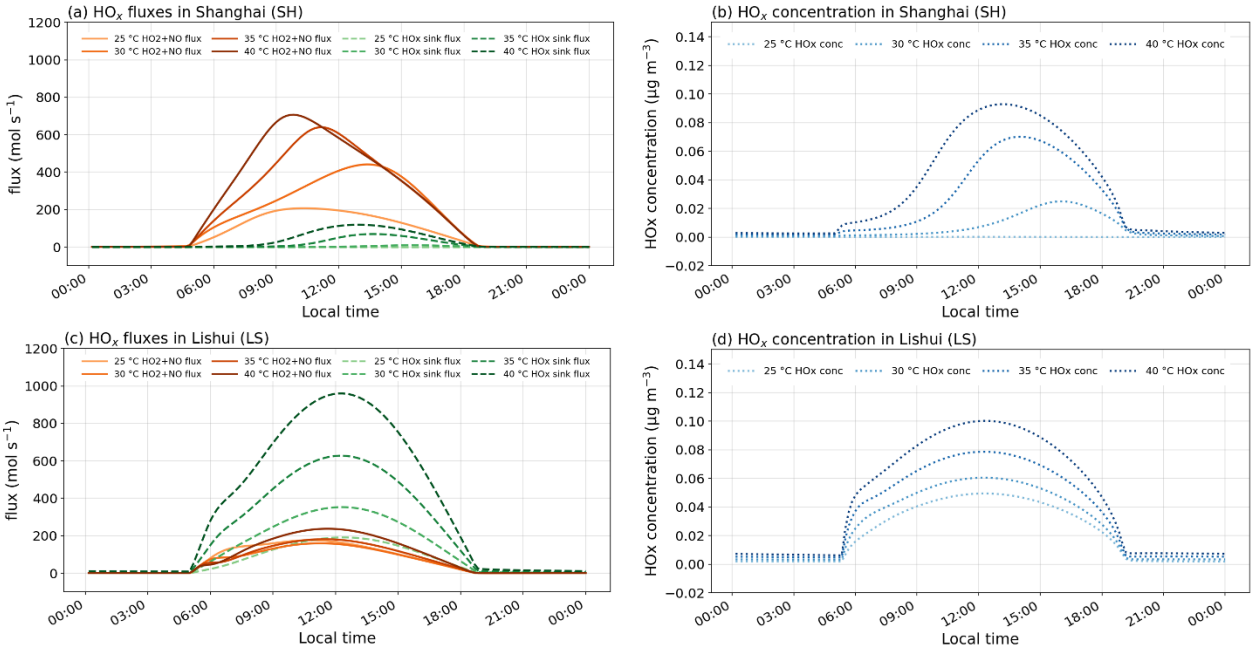

Figure 11. Diurnal HO_2+NO reaction, HO_x sink, and HO_x concentration at four temperatures. Panels (a-b) Shanghai and (c-d) Lishui. Solid orange lines show the HO_2+NO reaction flux (left axis, mol s^{-1}); dashed green lines show the total HO_x sink flux (left axis); dotted blue lines show HO_x concentration (right axis, μg m^{-3}). Each trio corresponds to a temperature scenario (25, 30, 35, 40 °C; lighter→darker with increasing temperature). Local time on the x-axis.

Figure 11 presents the diurnal evolution of the HO_2 + NO production flux (solid orange), the aggregate HOx-termination ("sink") flux (green dashed; e.g. OH + NO_2 + M, HO_2 + RO_2/HO_2), and the HOx concentration (blue dotted; right axis) at four imposed temperatures. As shown in Fig. 9, the HO_2 and NO reaction is the dominant O_3 chemical production pathway in both environments. HO_x sink reactions terminate O_3 formation, while HO_x is widely used as a proxy for the atmosphere's oxidising capacity, with OH controlling daytime oxidative processing (Feng et al., 2021); moreover, net ozone formation scales with the peroxy-NO reactions, so higher HOx—especially HO_2—correlates with stronger photochemical O_3 production (Archibald et al., 2020a; Pusede et al., 2015).

In both panels, chemical activity is tightly bound to daylight: fluxes are negligible at night, rise sharply after sunrise, peak near local noon-early afternoon, and collapse after sunset, reflecting the photochemical control of radical production.

In Shanghai (Fig. 11a-b), warming mainly strengthens the HO_x-driven O_x production. With increasing temperature, the daytime HO_2 + NO production flux (solid curves) increases strongly, and the peak HO_x concentrations (blue dotted curves, right axis)

https://doi.org/10.5194/egusphere-2026-836
Preprint. Discussion started: 12 March 2026

also increase, indicating more efficient radical recycling and a faster O_3 production cycle at higher T. The HO_x termination flux (green dashed curves) also grows with temperature, but the enhancement remains much smaller than the HO_2 + NO pathway throughout the day, so the temperature increase shows a more substantial impact on including more HO_x in O_x formation instead of facilitating the HO_x sink pathway. At T < 30 °C, both HO_x levels and the sink are low, implying that primary radical production is weak and the O_3 production cycle can be slow.

In Lishui (Fig. 11c-d), the behaviour is significantly different. Across the temperature range, the HO_x sink plays a much larger role, and at T ≥ 30 °C, its magnitude exceeds the HO_2 + NO flux. Interpreted in the context of the O_3 chemical cycle, this means a larger fraction of the available HO_x is channelled into termination rather than propagation. Even so, HO_x concentrations remain high from 25 to 40 °C, indicating efficient radical production; the high sink simply prevents those radicals from translating into proportionally larger HO_2 + NO rates.

Together, the panels show that warming enhances radical activity in both environments, but the partitioning between propagation and termination is site dependent: Shanghai exhibits production-dominated HO_x cycling that favours O_3 formation at high temperature, whereas Lishui exhibits sink-dominated cycling, consistent with background conditions where O_3 production is constrained by NO_x rather than HO_x availability.

https://doi.org/10.5194/egusphere-2026-836
Preprint. Discussion started: 12 March 2026

4 Conclusions

This study quantitatively evaluated the summertime temperature responses of ground-level ozone (O_3) across the Yangtze River Delta (YRD) and diagnosed how temperature-dependent O_x chemistry modulates surface O_3 using targeted UKCA Box experiments. We combined site observations from the 2022 summer in an urban megacity (Shanghai) and a rural region (Lishui) with a suite of experiments that separated the roles of chemical kinetics, temperature-dependent biogenic emissions, diurnal thermal structure, and humidity. Furthermore, we examined the O_x budget, PAN thermolysis, and the HO_x cycle to identify the mechanisms underlying the observed temperature sensitivities. We highlight that urban-rural differences largely exist in the intensity, process, and mechanism of ground-level O_3 temperature responses.

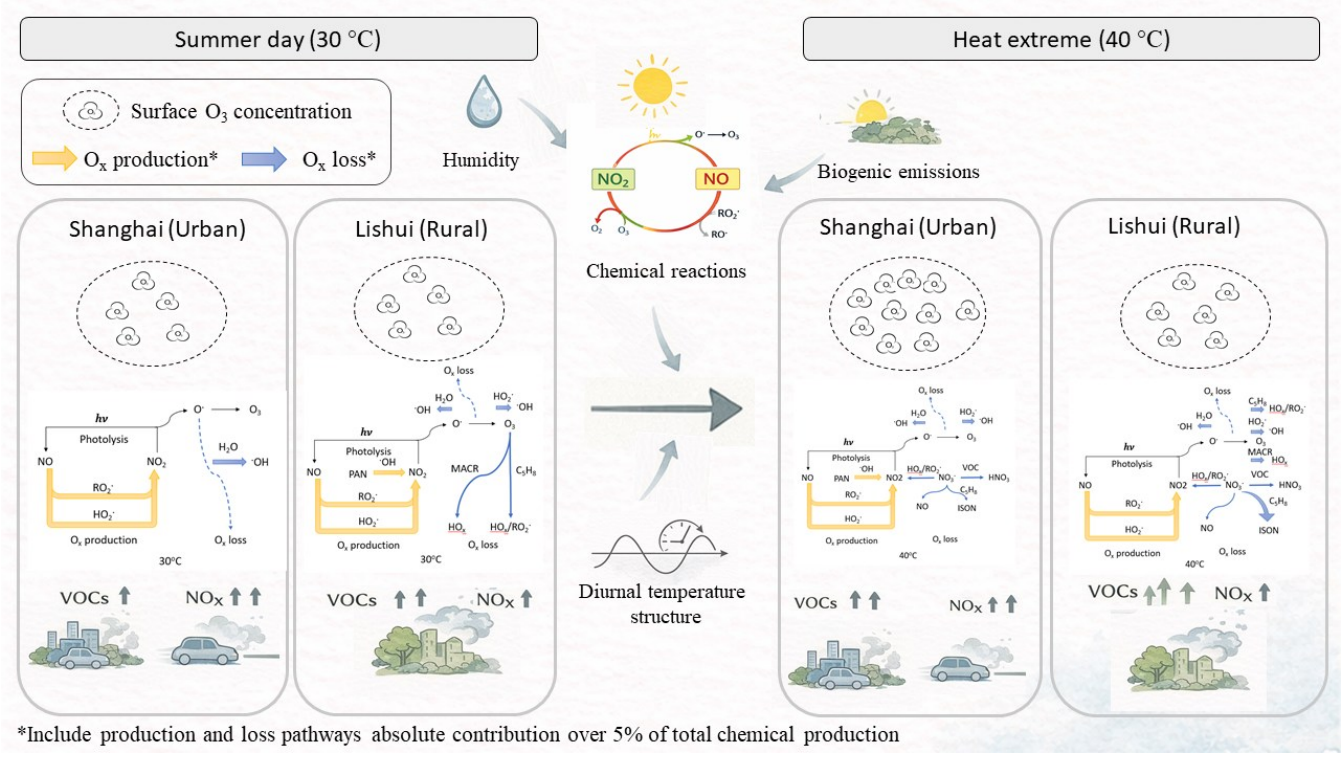

Figure 12. Conceptual summary of the mechanisms controlling surface ozone under typical summer conditions (30 °C; left) and heat extremes (40 °C; right) in Shanghai (urban) and Lishui (rural).

Summertime daily maximum observations showed robust, positive O_3-temperature relationships in both regions, stronger in Shanghai than in Lishui (mean JJA ΔO_{3max}-ΔT_{max} = 7.27 vs 3.36 μg m^{-3} $°C^{-1}$). Heatwave slopes remained positive in Lishui, but were statistically uncertain in Shanghai due to the limited number of events and larger variance at the low tail. Two-dimensional T-RH maps revealed that O_3 increases with temperature and decreases with relative humidity (RH). Because RH falls by ~2.4-3.2% RH per °C, part of the apparent temperature signal is mediated by drying.

https://doi.org/10.5194/egusphere-2026-836
Preprint. Discussion started: 12 March 2026

Factorial experiments isolated (i) net temperature-dependent chemical effects (Ori), (ii) the diurnal temperature cycle (D), (iii) temperature-dependent isoprene emissions (ft), and (iv) their combination (Dft), under fixed- and variable-RH assumptions (FRH/VRH). In Shanghai, the isoprene temperature response explained ~70 % of the observed ΔO_{3max} from 30 to 40 °C, with the diurnal cycle contributing ~10 % and residual kinetics accounting for ~20 %. Below 30 °C, observations aligned more closely with Ori/D, suggesting that unresolved meteorological controls (in the box model) (e.g., diurnal and day-to-day variation in boundary layer depth, transport/mixing into and out of the box) can offset the temperature sensitivity of isoprene emissions at lower temperatures. In Lishui, chemical temperature responses, i.e. peroxy-radical chemistry (HO_2/RO_2+NO), accounted for ~80 % of the 30 to 40 °C increase, while isoprene's temperature dependence contributed only ~10 %, consistent with a NO_x-limited rural regime. Allowing RH to co-vary with T reduced the apparent "thermal chemistry" contribution by ~35% in Lishui and ~20% in Shanghai, underscoring the need to treat T and RH jointly when diagnosing or projecting the climate penalty.

O_x budgets showed HO_2+NO as the leading production pathway in Shanghai, with RO_2+NO gaining importance toward 40 °C. In Lishui, the daily contribution of RO_2 + NO (including CH_3O_2 and other RO_2 species) to O_x production exceeds HO_2+NO, and the value doubles from 25 to 40 °C. On the loss side, $O(^1D)+H_2O$ dominates chemical destruction at both sites at temperatures from 25 to 35 °C, whereas O_3 + alkene reactions dominate at temperatures above 35 °C in Lishui. Deposition and physical transport remain the largest total O_x sink. For PAN, its thermolysis increased monotonically with temperature at both sites, implying stronger thermal NO_x recycling on hot afternoons; PAN concentrations declined with temperature in Lishui (loss outpaces production) but rose from 25 to 35 °C then fell at 40 °C in Shanghai, indicating that urban production can sustain PAN until very high temperatures when thermolysis and oxidant constraints dominate and imply potential threshold of PAN as NO_x source above 40 °C. HO_x diagnostics showed production-dominated cycling in Shanghai (HO_2+NO and [HO_x] increase with T; sink modest) versus sink-dominated cycling in Lishui above ~30 °C (high HO_x sink), reinforcing the regime contrast. Our site-scale attribution complements recent global UKCA applications with enhanced VOC chemistry over China that reproduced peak O_3 in industrial regions, identified VOC-limited behaviour in most megacity clusters, and demonstrated that NO_x-only controls can increase O_3 in VOC-limited environments. In contrast, VOC controls (or combined controls) are effective in reducing O_3. Read in that context, our findings sharpen the process basis for the YRD:

(i) In Shanghai-like urban conditions, temperature-amplified BVOC reactivity is a first-order lever of O_3 on hot days; mitigating the climate penalty therefore requires simultaneous NO_x reductions and targeted VOC management, which corresponds to previous urban O_3 formation studies (Gu et al., 2020; Liu et al., 2021b). Particularly, thoughtful urban greening (species selection/placement - i.e., low VOC emitters) is especially emphasised in this study, alongside improved representation of RH-stomata coupling in deposition schemes.

https://doi.org/10.5194/egusphere-2026-836
Preprint. Discussion started: 12 March 2026

(ii) In Lishui-like rural conditions, O_3 sensitivity is governed primarily by radical-NO_x chemistry and thermal PAN-NO_x cycling; NO_x reductions remain the most robust pathway to limit warming-induced O_3 amplification, while VOC reductions have a smaller marginal benefit.

(iii) Because RH and T co-vary, evaluations that ignore RH changes are likely to over-attribute the temperature effect to kinetic partitioning and understate deposition-mediated sinks. Multi-city analyses have reported a robust negative correlation between RH (or absolute humidity) and surface O_3, indicating that moist conditions systematically suppress O_3 compared with dry, hot weather (Li et al., 2021). In the present work, even with dry-deposition parameterisations held fixed, we find that changes in humidity alone substantially modify the O_x budget through $O(^1D)+H_2O$ loss and HO_x-NO_x cycling, implying that humidity-driven chemical effects can be a major contributor to the apparent climate penalty, independent of any RH influence on stomatal or surface uptake.

Our conclusions are based on one exceptionally hot summer (2022) and inherit limitations from the heatwave sample size and the 0-D nature of the box model (no transport, clouds, or physical feedbacks). Nevertheless, agreement across independent diagnostics—JJA and heatwave regressions, binned ΔO_3 comparisons, O_x/PAN/HO_x budgets—builds a consistent mechanistic picture. In summary, summertime O_3 in the YRD increases with temperature for regime-specific reasons: BVOC-driven in the urban core, radical-NO_x-driven in the rural area, and materially modulated by humidity conditions. Although the quantitative sensitivities documented here are specific to the YRD emissions-meteorology setting, the underlying mechanisms, such as temperature-enhanced BVOC reactivity in VOC-limited urban air, radical-NO_x control and PAN-mediated NO_x recycling in rural air, and the damping role of high humidity, are consistent with process-based analyses for other polluted mid-latitude regions (e.g. eastern North America and Europe) and are therefore expected to be qualitatively applicable in similar regimes and climate settings.

The UKCA Box provides a transparent, observation-constrained framework for attributing these responses to processes within O_x chemistry, offering actionable guidance for heat-resilient emission controls and serving as a bridge to regional policy analyses informed by broader UKCA simulations. Priorities for future work include (a) evaluating the performance of the UKCA model on reproducing the meteorological contribution to surface O_3 in different types of summer days, and (b) the contribution of meteorological fields and precursor emissions during heatwaves, non-heatwave hot days and summer days.

https://doi.org/10.5194/egusphere-2026-836
Preprint. Discussion started: 12 March 2026

Data availability

The data used in this study are available from the corresponding author upon request (chang.su@ed.ac.uk).

Supplement

The supplement related to this article is available online at: .

Author contributions

CS prepared the dataset, performed UKCA Box Model simulations, specified the corresponding model settings, conducted the analysis, and wrote the paper. DS and MB helped design the research, guided the data analysis, contributed to the scientific discussions, and helped with the final version of the paper. JW performed the UKESM-AMIP simulations, contributed to the corresponding model configuration, and commented on the final version of the paper.

Competing interests

The contact author has declared that neither they nor their co-authors have any competing interests.

Disclaimer

Publisher's note: Copernicus Publications remains neutral with regard to jurisdictional claims in published maps and institutional affiliations.

Acknowledgements

We acknowledge the guidance during setting up the UKCA Box Model from Prof. N. Luke Abraham, National Centre for Atmospheric Science.

Financial support

This research has been supported by the Natural Environment Research Council (UKRI/NERC) and the UK Department for Energy Security and Net Zero (grant no. NE/X012735/1).

https://doi.org/10.5194/egusphere-2026-836
Preprint. Discussion started: 12 March 2026

References

An, J., et al.: Emission inventory of air pollutants and chemical speciation for specific anthropogenic sources based on local measurements in the Yangtze River Delta region, China, Atmos. Chem. Phys., 21, 2003-2025, 10.5194/acp-21-2003-2021, 2021.

Archibald, A. T., et al.: On the changes in surface ozone over the twenty-first century: sensitivity to changes in surface temperature and chemical mechanisms, Philosophical Transactions of the Royal Society A: Mathematical, Physical and Engineering Sciences, 378, 20190329, https://doi.org/10.1098/rsta.2019.0329, 2020a.

Archibald, A. T., et al.: Description and evaluation of the UKCA stratosphere–troposphere chemistry scheme (StratTrop vn 1.0) implemented in UKESM1, Geosci. Model Dev., 13, 1223-1266, 10.5194/gmd-13-1223-2020, 2020b.

Bates, K. H. and Jacob, D. J.: An Expanded Definition of the Odd Oxygen Family for Tropospheric Ozone Budgets: Implications for Ozone Lifetime and Stratospheric Influence, Geophysical Research Letters, 47, e2019GL084486, https://doi.org/10.1029/2019GL084486, 2020.

Bloomer, B. J., Vinnikov, K. Y., and Dickerson, R. R.: Changes in seasonal and diurnal cycles of ozone and temperature in the eastern U.S, Atmospheric Environment, 44, 2543-2551, https://doi.org/10.1016/j.atmosenv.2010.04.031, 2010.

Chen, P., et al.: Characteristics of VOCs and their Potentials for O3 and SOA Formation in a Medium-sized City in Eastern China, Aerosol and Air Quality Research, 22, 210239, http://dx.doi.org/10.4209/aaqr.210239, 2022.

Cleary, P. A., et al.: Observations of total peroxy nitrates and aldehydes: measurement interpretation and inference of OH radical concentrations, Atmos. Chem. Phys., 7, 1947-1960, 10.5194/acp-7-1947-2007, 2007.

Clifton, O. E., et al.: Influence of Dynamic Ozone Dry Deposition on Ozone Pollution, Journal of Geophysical Research: Atmospheres, 125, e2020JD032398, https://doi.org/10.1029/2020JD032398, 2020a.

Clifton, O. E., et al.: Dry Deposition of Ozone Over Land: Processes, Measurement, and Modeling, Reviews of Geophysics, 58, e2019RG000670, https://doi.org/10.1029/2019RG000670, 2020b.

Cohen, A. J., et al.: Estimates and 25-year trends of the global burden of disease attributable to ambient air pollution: an analysis of data from the Global Burden of Diseases Study 2015, The Lancet, 389, 1907-1918, https://doi.org/10.1016/S0140-6736(17)30505-6, 2017.

Dee, D. P., et al.: The ERA-Interim reanalysis: configuration and performance of the data assimilation system, Quarterly Journal of the Royal Meteorological Society, 137, 553-597, https://doi.org/10.1002/qj.828, 2011.

Duc, H. N., et al.: Study of Planetary Boundary Layer, Air Pollution, Air Quality Models and Aerosol Transport Using Ceilometers in New South Wales (NSW), Australia, 10.3390/atmos13020176, 2022.

Ebi, K. L., et al.: Hot weather and heat extremes: health risks, The Lancet, 398, 698-708, https://doi.org/10.1016/S0140-6736(21)01208-3, 2021.

https://doi.org/10.5194/egusphere-2026-836
Preprint. Discussion started: 12 March 2026

Engdaw, M. M., Ballinger, A. P., Hegerl, G. C., and Steiner, A. K.: Changes in temperature and heat waves over Africa using observational and reanalysis data sets, International Journal of Climatology, 42, 1165-1180, https://doi.org/10.1002/joc.7295, 2022.

Feng, T., et al.: Assessment of Atmospheric Oxidizing Capacity Over the Beijing-Tianjin-Hebei (BTH) Area, China, Journal of Geophysical Research: Atmospheres, 126, e2020JD033834, https://doi.org/10.1029/2020JD033834, 2021.

Fischer, E. M. and Schär, C.: Consistent geographical patterns of changes in high-impact European heatwaves, Nature Geoscience, 3, 398-403, 10.1038/ngeo866, 2010.

Fischer, E. V., et al.: Atmospheric peroxyacetyl nitrate (PAN): a global budget and source attribution, Atmos. Chem. Phys., 14, 2679-2698, 10.5194/acp-14-2679-2014, 2014.

Forouzanfar, M. H., et al.: Global, regional, and national comparative risk assessment of 79 behavioural, environmental and occupational, and metabolic risks or clusters of risks in 188 countries, 1990–2013: a systematic analysis for the Global Burden of Disease Study 2013, The Lancet, 386, 2287-2323, 10.1016/S0140-6736(15)00128-2, 2015.

García-Martínez, I. and Bollasina, M.: Identifying the evolving human imprint on heat wave trends over the United States and Mexico, Environmental Research Letters, 16, 094039, 10.1088/1748-9326/ac1edb, 2021.

Gong, Y., et al.: Assessing Changes in the Ecosystem Services Value in Response to Land-Use/Land-Cover Dynamics in Shanghai from 2000 to 2020, 10.3390/ijerph191912080, 2022.

Gu, C., et al.: Investigation on the urban ambient isoprene and its oxidation processes, Atmospheric Environment, 270, 118870, https://doi.org/10.1016/j.atmosenv.2021.118870, 2022.

Gu, Y., et al.: Observed dependence of surface ozone on increasing temperature in Shanghai, China, Atmospheric Environment, 221, 117108, https://doi.org/10.1016/j.atmosenv.2019.117108, 2020.

Guenther, A. B., et al.: The Model of Emissions of Gases and Aerosols from Nature version 2.1 (MEGAN2.1): an extended and updated framework for modeling biogenic emissions, Geosci. Model Dev., 5, 1471-1492, 10.5194/gmd-5-1471-2012, 2012.

Hoesly, R. M., et al.: Historical (1750–2014) anthropogenic emissions of reactive gases and aerosols from the Community Emissions Data System (CEDS), Geosci. Model Dev., 11, 369-408, 10.5194/gmd-11-369-2018, 2018.

Hu, L., et al.: Global budget of tropospheric ozone: Evaluating recent model advances with satellite (OMI), aircraft (IAGOS), and ozonesonde observations, Atmospheric Environment, 167, 323-334, https://doi.org/10.1016/j.atmosenv.2017.08.036, 2017.

Jin, X. and Holloway, T.: Spatial and temporal variability of ozone sensitivity over China observed from the Ozone Monitoring Instrument, Journal of Geophysical Research: Atmospheres, 120, 7229-7246, https://doi.org/10.1002/2015JD023250, 2015.

Kalisa, E., et al.: Temperature and air pollution relationship during heatwaves in Birmingham, UK, Sustainable Cities and Society, 43, 111-120, https://doi.org/10.1016/j.scs.2018.08.033, 2018.

Kavassalis, S. C. and Murphy, J. G.: Understanding ozone-meteorology correlations: A role for dry deposition, Geophysical Research Letters, 44, 2922-2931, https://doi.org/10.1002/2016GL071791, 2017.

https://doi.org/10.5194/egusphere-2026-836
Preprint. Discussion started: 12 March 2026

Li, M., et al.: Large scale control of surface ozone by relative humidity observed during warm seasons in China, Environmental Chemistry Letters, 19, 3981-3989, 10.1007/s10311-021-01265-0, 2021.

Li, M., et al.: Persistent growth of anthropogenic non-methane volatile organic compound (NMVOC) emissions in China during 1990–2017: drivers, speciation and ozone formation potential, Atmos. Chem. Phys., 19, 8897-8913, 10.5194/acp-19-8897-2019, 2019.

丽水简介 [Introduction of Lishui; in Chinese]: http://tjj.lishui.gov.cn/col/col1229215882/index.html, last access: 17 Sep 2025.

Liu, H., et al.: Ground-level ozone pollution and its health impacts in China, Atmospheric Environment, 173, 223-230, https://doi.org/10.1016/j.atmosenv.2017.11.014, 2018.

Liu, Y., et al.: Formation of peroxyacetyl nitrate (PAN) and its impact on ozone production in the coastal atmosphere of Qingdao, North China, Science of The Total Environment, 778, 146265, https://doi.org/10.1016/j.scitotenv.2021.146265, 2021a.

Liu, Z., et al.: Contrasting chemical environments in summertime for atmospheric ozone across major Chinese industrial regions: the effectiveness of emission control strategies, Atmos. Chem. Phys., 21, 10689-10706, https://acp.copernicus.org/articles/21/10689/2021/, 2021b.

Ma, M., et al.: Development and Assessment of a High-Resolution Biogenic Emission Inventory from Urban Green Spaces in China, Environmental Science & Technology, 56, 175-184, https://doi.org/10.1021/acs.est.1c06170, 2022a.

Ma, X., et al.: OH and HO2 radical chemistry at a suburban site during the EXPLORE-YRD campaign in 2018, Atmos. Chem. Phys., 22, 7005-7028, 10.5194/acp-22-7005-2022, 2022b.

McDuffie, E. E., et al.: Influence of oil and gas emissions on summertime ozone in the Colorado Northern Front Range, Journal of Geophysical Research: Atmospheres, 121, 8712-8729, https://doi.org/10.1002/2016JD025265, 2016.

Meehl, G. A., et al.: Future heat waves and surface ozone, Environmental Research Letters, 13, 064004, https://dx.doi.org/10.1088/1748-9326/aabcdc, 2018.

Meng, X., et al.: Chemical drivers of ozone change in extreme temperatures in eastern China, Science of The Total Environment, 874, 162424, https://doi.org/10.1016/j.scitotenv.2023.162424, 2023.

Mulcahy, J. P., et al.: Description and evaluation of aerosol in UKESM1 and HadGEM3-GC3.1 CMIP6 historical simulations, Geosci. Model Dev., 13, 6383-6423, 10.5194/gmd-13-6383-2020, 2020.

Nguyen, D.-H., et al.: Tropospheric ozone and NOx: A review of worldwide variation and meteorological influences, Environmental Technology & Innovation, 28, 102809, https://doi.org/10.1016/j.eti.2022.102809, 2022.

Ning, G., Wardle, D. A., and Yim, S. H. L.: Suppression of Ozone Formation at High Temperature in China: From Historical Observations to Future Projections, Geophysical Research Letters, 49, e2021GL097090, https://doi.org/10.1029/2021GL097090, 2022.

Nolte, C. G., et al.: Regional temperature-ozone relationships across the U.S. under multiple climate and emissions scenarios, Journal of the Air & Waste Management Association, 71, 1251-1264, 10.1080/10962247.2021.1970048, 2021.

https://doi.org/10.5194/egusphere-2026-836
Preprint. Discussion started: 12 March 2026

Olivier, J., et al.: Present and future surface emissions of atmospheric compounds (POET Report #2), EU project EVK2-1999-00011 (POET), 2003.

Otero, N., Rust, H. W., and Butler, T.: Temperature dependence of tropospheric ozone under NOx reductions over Germany, Atmospheric Environment, 253, 118334, https://doi.org/10.1016/j.atmosenv.2021.118334, 2021.

Pacifico, F., et al.: Evaluation of a photosynthesis-based biogenic isoprene emission scheme in JULES and simulation of isoprene emissions under present-day climate conditions, Atmos. Chem. Phys., 11, 4371-4389, 10.5194/acp-11-4371-2011, 2011.

Pfister, G. G., et al.: Projections of future summertime ozone over the U.S, Journal of Geophysical Research: Atmospheres, 119, 5559-5582, https://doi.org/10.1002/2013JD020932, 2014.

Phillips, G. J., et al.: Peroxyacetyl nitrate (PAN) and peroxyacetic acid (PAA) measurements by iodide chemical ionisation mass spectrometry: first analysis of results in the boreal forest and implications for the measurement of PAN fluxes, Atmos. Chem. Phys., 13, 1129-1139, 10.5194/acp-13-1129-2013, 2013.

Pope, R. J., et al.: Investigation of the summer 2018 European ozone air pollution episodes using novel satellite data and modelling, Atmos. Chem. Phys., 23, 13235-13253, https://doi.org/10.5194/acp-23-13235-2023, 2023.

Pusede, S. E., Steiner, A. L., and Cohen, R. C.: Temperature and Recent Trends in the Chemistry of Continental Surface Ozone, Chemical Reviews, 115, 3898-3918, https://doi.org/10.1021/cr5006815, 2015.

Ren, J., Guo, F., and Xie, S.: Diagnosing ozone–NOx–VOC sensitivity and revealing causes of ozone increases in China based on 2013–2021 satellite retrievals, Atmos. Chem. Phys., 22, 15035-15047, 10.5194/acp-22-15035-2022, 2022.

2023 年上海市国民经济和社会发展统计公报 [Statistical Communiqué of Shanghai on the 2023 National Economic and Social Development; in Chinese]: https://tjj.sh.gov.cn/tjgb/20240321/f66c5b25ce604a1f9af755941d5f454a.html, last access: 17 Sep 2025.

Shen, L., Mickley, L. J., and Gilleland, E.: Impact of increasing heat waves on U.S. ozone episodes in the 2050s: Results from a multimodel analysis using extreme value theory, Geophysical Research Letters, 43, 4017-4025, https://doi.org/10.1002/2016GL068432, 2016.

Sillman, S.: The relation between ozone, NOx and hydrocarbons in urban and polluted rural environments, Atmospheric Environment, 33, 1821-1845, https://doi.org/10.1016/S1352-2310(98)00345-8, 1999.

Simon, H., et al.: Ozone Trends Across the United States over a Period of Decreasing NOx and VOC Emissions, Environmental Science & Technology, 49, 186-195, https://doi.org/10.1021/es504514z, 2015.

Solberg, S., et al.: European surface ozone in the extreme summer 2003, Journal of Geophysical Research: Atmospheres, 113, https://doi.org/10.1029/2007JD009098, 2008.

Steiner, A. L., et al.: Influence of future climate and emissions on regional air quality in California, Journal of Geophysical Research: Atmospheres, 111, https://doi.org/10.1029/2005JD006935, 2006.

https://doi.org/10.5194/egusphere-2026-836
Preprint. Discussion started: 12 March 2026

Steiner, A. L., et al.: Observed suppression of ozone formation at extremely high temperatures due to chemical and biophysical feedbacks, Proceedings of the National Academy of Sciences, 107, 19685-19690, https://doi.org/10.1073/pnas.1008336107, 2010.

Stella, P., et al.: Ozone deposition onto bare soil: A new parameterisation, Agricultural and Forest Meteorology, 151, 669-681, https://doi.org/10.1016/j.agrformet.2011.01.015, 2011.

Sun, W., Hess, P., and Liu, C.: The impact of meteorological persistence on the distribution and extremes of ozone, Geophysical Research Letters, 44, 1545-1553, https://doi.org/10.1002/2016GL071731, 2017.

Sun, Y., et al.: Examining the joint effects of heatwaves, air pollution, and green space on the risk of preterm birth in California, Environmental Research Letters, 15, 104099, 10.1088/1748-9326/abb8a3, 2020.

Szopa, S., et al.: Short-Lived Climate Forcers, in: Climate Change 2021: The Physical Science Basis. Contribution of Working Group I to the Sixth Assessment Report of the Intergovernmental Panel on Climate Change, edited by: Masson-Delmotte, V., Zhai, P., Pirani, A., Connors, S. L., Péan, C., Berger, S., Caud, N., Chen, Y., Goldfarb, L., Gomis, M. I., Huang, M., Leitzell, K., Lonnoy, E., Matthews, J. B. R., Maycock, T. K., Waterfield, T., Yelekçi, O., Yu, R., and Zhou, B., Cambridge University Press, Cambridge, UK; New York, NY, USA, 817-922, 10.1017/9781009157896.008, 2021.

Tang, Y., et al.: Land ecological protection polices improve ecosystem services: A case study of Lishui, China, Frontiers in Environmental Science, Volume 10 - 2022, 2022.

Telford, P. J., et al.: Implementation of the Fast-JX Photolysis scheme (v6.4) into the UKCA component of the MetUM chemistry-climate model (v7.3), Geosci. Model Dev., 6, 161-177, 10.5194/gmd-6-161-2013, 2013.

Box model (UKCA Wiki): https://www.ukca.ac.uk/wiki/index.php/Box_model, last access: 6 Oct 2025.

Utembe, S. R., et al.: Hot Summers: Effect of Extreme Temperatures on Ozone in Sydney, Australia, https://doi.org/10.3390/atmos9120466, 2018.

Walters, D., et al.: The Met Office Unified Model Global Atmosphere 7.0/7.1 and JULES Global Land 7.0 configurations, Geosci. Model Dev., 12, 1909-1963, 10.5194/gmd-12-1909-2019, 2019.

Wang, M., et al.: Investigating the Seasonal Effect of Climatic Factors on Evapotranspiration in the Monsoon Climate Zone: A Case Study of the Yangtze River Basin, 10.3390/atmos14081282, 2023.

Wang, P., et al.: North China Plain as a hot spot of ozone pollution exacerbated by extreme high temperatures, Atmos. Chem. Phys., 22, 4705-4719, https://doi.org/10.5194/acp-22-4705-2022, 2022a.

Wang, W., et al.: Long-term trend of ozone pollution in China during 2014–2020: distinct seasonal and spatial characteristics and ozone sensitivity, Atmos. Chem. Phys., 22, 8935-8949, 10.5194/acp-22-8935-2022, 2022b.

Wesely, M. L.: Parameterization of surface resistances to gaseous dry deposition in regional-scale numerical models, Atmospheric Environment (1967), 23, 1293-1304, https://doi.org/10.1016/0004-6981(89)90153-4, 1989.

Wilson, B., et al.: Characterizing changes in extreme ozone levels under 2050s climate conditions: An extreme-value analysis in California, Atmospheric Environment: X, 16, 100195, https://doi.org/10.1016/j.aeaoa.2022.100195, 2022.

Climate change and heatwaves: https://wmo.int/content/climate-change-and-heatwaves, last access: 2 June 2025.

https://doi.org/10.5194/egusphere-2026-836
Preprint. Discussion started: 12 March 2026

Wu, K., et al.: Estimation of biogenic VOC emissions and their corresponding impact on ozone and secondary organic aerosol formation in China, Atmospheric Research, 231, 104656, https://doi.org/10.1016/j.atmosres.2019.104656, 2020.

Wu, S., et al.: Effects of 2000–2050 global change on ozone air quality in the United States, Journal of Geophysical Research: Atmospheres, 113, https://doi.org/10.1029/2007JD008917, 2008.

Wu, W., et al.: Temperature-Dependent Evaporative Anthropogenic VOC Emissions Significantly Exacerbate Regional Ozone Pollution, Environmental Science & Technology, 58, 5430-5441, 10.1021/acs.est.3c09122, 2024.

Wu, Y., et al.: Observation of heat wave effects on the urban air quality and PBL in New York City area, Atmospheric Environment, 218, 117024, https://doi.org/10.1016/j.atmosenv.2019.117024, 2019.

Xia, Y., et al.: Concurrent hot extremes and high ultraviolet radiation in summer over the Yangtze Plain and their possible impact on surface ozone, Environmental Research Letters, 17, 064001, 10.1088/1748-9326/ac6c3c, 2022.

Yamada, H.: Contribution of evaporative emissions from gasoline vehicles toward total VOC emissions in Japan, Science of The Total Environment, 449, 143-149, https://doi.org/10.1016/j.scitotenv.2013.01.045, 2013.

Zhang, J., et al.: Impacts of compound extreme weather events on ozone in the present and future, Atmos. Chem. Phys., 18, 9861-9877, 10.5194/acp-18-9861-2018, 2018.

Zhang, L., Brook, J. R., and Vet, R.: A revised parameterization for gaseous dry deposition in air-quality models, Atmos. Chem. Phys., 3, 2067-2082, 10.5194/acp-3-2067-2003, 2003.

Zhao, A., Bollasina, M. A., and Stevenson, D. S.: Strong Influence of Aerosol Reductions on Future Heatwaves, Geophysical Research Letters, 46, 4913-4923, https://doi.org/10.1029/2019GL082269, 2019.